



## **School of Chemistry**

### The Fabrication and Electrochemical Analysis of Nanostructured Diamond for Electrochemical Applications

Jessica Scott

**This thesis is submitted in partial fulfilment of the requirements for the Honours Degree  
of MSci at the University of Bristol**

[Supervisor] Paul. W. May

[Second Assessor] David. J. Fermin

[Section] Physical & Theoretical



# Abstract

Nanostructured boron-doped diamond (BDD) electrodes present an exciting opportunity for advancing electrochemical technologies that require high chemical stability and enhanced surface activity. While micro- and nanostructured approaches on carbon-based electrodes have been well documented, precise control over morphology and its influence on electrochemical performance remains insufficiently understood. Furthermore, the application of nanostructured BDD electrodes for reactions such as furfural (FF) oxidation, is largely underexplored. This project aimed to address these gaps by investigating how electron beam lithography (EBL), combined with surface termination treatments can enhance the electrochemical properties of BDD electrodes for sustainable chemical applications.

Three EBL-BDD electrode designs were fabricated with varying structure densities to investigate the influence of surface morphology on electrochemical performance. Material characterisation by scanning electron microscopy (SEM) and laser Raman spectroscopy confirmed successful growth of nanocrystalline BDD films across all structures. Electrochemical characterisation in  $\text{KNO}_3$  solution, demonstrated substantial improvements in double-layer capacitance ( $C_{dl}$ ) with the highest performing electrode, EBL D-05, exhibiting a  $C_{dl}$  value 50.6 times greater than the average f-BDD reference. Surface area analysis further validated these findings, with relative effective surface area indicating up to a 25-fold increase over f-BDD. Oxygen termination treatments were also explored, with ozone treatment proving to be most effective relative to the hydrogen-terminated reference.

Preliminary application testing for FF oxidation was conducted in acidic media. The EBL D-22 electrode displayed promising activity, with an anodic peak at 1.6 V vs. Ag/AgCl, confirming catalytic activity towards FF oxidation.



## **Acknowledgements**

Firstly, I would like to express my sincere gratitude to Professor Paul May for his invaluable guidance and support throughout my project and allowing me to enter his lab and work alongside everyone in the BUDGies group.

I would also like to thank Kisty Mao for her constant assistance throughout this year, I truly believe I could not have completed this project without her encouragement, and I am honoured to have had her to guide me through my final year at Bristol. I have thoroughly enjoyed the time we have spent together working on this project. I would also like to thank Dr James Smith for his help with the operation of the Laser Raman.

Thank you to Professor David Fermin for allowing me to work in his Electrochemistry lab for the latter half of my project and helping me to understand the applications of my project and answering any questions I had. I would also like to thank Alex for providing the electrode equipment and generously offering his expertise.

Finally, I wish to express my heartfelt gratitude to my family and friends for their unwavering support throughout this year and the entirety of my degree at Bristol. I am deeply thankful to have been surrounded by such incredible people, whose encouragement during challenging times and shared celebrations have made this journey truly memorable.



# Table of Contents

Page

<b>List of Tables</b> .....	<b>i.</b>
<b>List of Figures</b> .....	<b>iii.</b>
<b>List of Abbreviations and Symbols</b> .....	<b>v.</b>

## **1. Introduction**

1.1. Microstructured Electrodes .....	1
1.2. Diamond in Electrochemistry .....	2
<b>1.2.1. Diamond Properties</b> .....	<b>2</b>
<b>1.2.2. Electrochemical Performance</b> .....	<b>3</b>
<b>1.2.3. Band Gap Theory</b> .....	<b>4</b>
<b>1.2.4. Semiconductors</b> .....	<b>5</b>
1.3. Fabrication Approaches for High Surface Area BDD Electrodes .....	7
<b>1.3.1. Top-Down Etching</b> .....	<b>7</b>
<b>1.3.2. Bottom-up growth</b> .....	<b>11</b>
1.4. CVD: Chemical Vapour Deposition.....	12
<b>1.4.1. Chemical Vapour Mixture</b> .....	<b>14</b>
<b>1.4.2. Microwave Plasma-Enhanced Chemical Vapour Deposition</b> .....	<b>14</b>
<b>1.4.3. Hot Filament Chemical Vapour Deposition</b> .....	<b>15</b>
1.5. Electrode Characterisation and Analysis .....	17
<b>1.5.1. Scanning Electron Microscopy</b> .....	<b>17</b>
<b>1.5.2. Laser Raman Spectroscopy</b> .....	<b>17</b>
<b>1.5.3. Electrical Conductivity</b> .....	<b>18</b>
<b>1.5.4. Double Layer Capacitance</b> .....	<b>18</b>
1.6. EBL-BDD Electrode Applications.....	20
<b>1.6.1. The Water Hydrolysis Reaction</b> .....	<b>20</b>
<b>1.6.2. Furfural Oxidation</b> .....	<b>22</b>
<b>1.6.3. Electrochemical Sensing</b> .....	<b>23</b>
1.7. Scope of the Project .....	24

## 2. Experimental

2.1.	EBL-Si Substrate Preparation .....	26
2.2.	EBL-Si Etching Process.....	16
2.3.	HFCVD.....	28
2.4.	Film Characterisation.....	29
2.5.	Electrochemical Analysis.....	29
<b>2.5.1.</b>	<b>Chemicals.....</b>	<b>29</b>
<b>2.5.2.</b>	<b>Electrodes.....</b>	<b>29</b>
<b>2.5.3.</b>	<b>Apparatus.....</b>	<b>30</b>
<b>2.5.3.</b>	<b>Oxygen Termination Treatment.....</b>	<b>31</b>
<b>2.5.4.</b>	<b>Furfural Oxidation.....</b>	<b>31</b>

## 3. Results and Discussion

3.1.	Material Characterisation.....	32
<b>3.1.1.</b>	<b>Determining the HFCVD Growth Time (SEM) .....</b>	<b>32</b>
<b>3.1.2.</b>	<b>Investigating Boron Concentration (Laser Raman) .....</b>	<b>35</b>
3.2.	Electrochemical Performance .....	37
<b>3.2.1.</b>	<b>Effect of Oxygen Termination Pre-Treatments .....</b>	<b>37</b>
<b>3.2.2.</b>	<b>EBL-BDD Double Layer Capacitance Performance .....</b>	<b>38</b>
<b>3.2.3.</b>	<b>Control f-BDD .....</b>	<b>41</b>
<b>3.2.4.</b>	<b>f-BDD vs. EBL-BDD .....</b>	<b>43</b>
<b>3.2.5.</b>	<b>Determinations of Surface Area.....</b>	<b>45</b>
3.3.	Furfural Oxidation .....	49
<b>3.3.1.</b>	<b>Activity of EBL-BDD for Furfural Oxidation.....</b>	<b>49</b>

## 4. Conclusions and Future Work

4.1.	Conclusions.....	52
4.2.	Future Work .....	53

## 5. Appendix

5.1. SEM images of EBL-Si with a) thickness ( $T$ ) <200 nm and b) pitch ( $P$ ) <500 nm. ....	56
5.2. Visible laser Raman spectra for black diamond (bD) electrodes fabricated for different growth times from 15-60 minutes.....	56
5.3. Visible Laser Raman spectra for each EBL-BDD electrode showing a significant first-order Si peak. ....	57
5.4. CV of 0.5 M H <sub>2</sub> SO <sub>4</sub> and 0.5 M H <sub>2</sub> SO <sub>4</sub> + 25 mM FF, $\nu = 100 \text{ mV s}^{-1}$ with EBL D-22 .....	57
<b>6. References .....</b>	<b>58</b>

# List of Tables

	<b>Page</b>
<b>Table 3.1:</b> Diamond film thickness and the gap between the nanostructured pillars after 30 minutes diamond growth. ....	33
<b>Table 3.2:</b> Diamond film thickness and the gap between the nanostructured pillars after 55 minutes diamond growth. ....	34
<b>Table 3.3:</b> Double-layer capacitance values for each oxygen termination treatment. ....	38
<b>Table 3.4:</b> Double-layer capacitance ( $C_{dl}$ ) values for each EBL BDD electrode in $\mu\text{F cm}^{-2}$ . ....	40
<b>Table 3.5:</b> Double-layer capacitance ( $C_{dl}$ ) values for each f-BDD sample giving an average value of $15.7 \mu\text{F cm}^{-2}$ . ....	42
<b>Table 3.6:</b> Double-layer capacitance ( $C_{dl}$ ) values for flat and nanostructured BDD electrodes, and their relative enhancement compared to flat BDD. ....	44
<b>Table 3.7:</b> Actual surface area ( $S_{Actual}$ ) of each BDD electrode. ....	46
<b>Table 3.8:</b> Relative effective surface area of each BDD electrode. ....	48

# List of Figures

	<b>Page</b>
<b>Figure 1.1:</b> The structure of diamond in both (a) ball and stick form and (b) chemical structure.....	2
<b>Figure 1.2:</b> Schematic diagrams of the crystal structures of cubic symmetry diamond structure (ABCABC) and hexagonal symmetry graphite structure (ABABAB) taken from <b>Ref. 4</b> .....	2
<b>Figure 1.3:</b> Simple visualisations of the {100} and {111} planes of crystal diamond taken from <b>Ref. 5</b> .....	3
<b>Figure 1.4:</b> Potential windows of different common electrodes. Redrawn using data from <b>Ref. 13</b> .....	4
<b>Figure 1.5:</b> The effect of B doping on the band gap of diamond. Without the acceptor level, to make diamond conductive electrons would need to be excited from the valence band to the conduction band across 5.5 eV but the acceptor level greatly decreases this gap to only 0.37 eV for electrons to jump and give a conducting material. ....	5
<b>Figure 1.6:</b> Mechanism for the fabrication of diamond nanowires from Ni nanoparticles using RIE redrawn from <b>Ref. 29</b> .....	7
<b>Figure 1.7:</b> SEM image of vertically aligned BDD nanowires using diamond nanoparticles as masks taken from <b>Ref. 28</b> . ....	8
<b>Figure 1.8:</b> Top view (a) and (b) and tilt-view (c) and (d) SEM images of VACNT forests taken from <b>Ref. 31</b> .....	9
<b>Figure 1.9:</b> SEM image of bSi columns after a coating of BDD. ....	16
<b>Figure 1.10a:</b> Mechanism for the dissociation of H <sub>2</sub> gas <i>in situ</i> . ....	16
<b>Figure 1.10b:</b> Mechanism for the removal of hydrogen from surface carbon. ....	16
<b>Figure 1.10c:</b> Mechanism for the addition of methyl radical to activated surface carbon radical.....	16
<b>Figure 1.11:</b> Schematic diagram of a MWCVD setup taken from <b>Ref. 65</b> .....	16
<b>Figure 1.12:</b> Schematic diagram of a HFCVD set up taken from <b>Ref. 72</b> .....	16
<b>Figure 1.13:</b> The electrical double layer drawn with information from <b>Ref. 82</b> . (pg. 13).....	18

<b>Figure 1.14:</b> Furfural oxidation to furoic acid (FCA), maleic acid (MA), 5-hydroxy-2(5 <i>H</i> )-furanone (HFN), and furandicarboxylic acid (FDCA). Redrawn from information in <b>Ref. 105</b> .....	23
<b>Figure 2.1:</b> Schematic representation of the etching process used in the School of Physics University Cleanroom. ....	27
<b>Figure 2.2:</b> The parameters used for each EBL design: pitch ( <i>P</i> ) and thickness ( <i>T</i> ).....	27
<b>Figure 2.3:</b> Image of the electrode holder used for f-BDD and EBL-BDD samples. The electrode holder was provided by Alex Black. ....	30
<b>Figure 2.4:</b> (a) The electrochemical cell. Left: Ag/AgCl reference electrode; centre: BDD working electrode in electrode holder designed by Alex Black; right: glassy carbon counter electrode. (b) $\mu$ Autolab Type III potentiostat and computer set up. ....	30
<b>Figure 3.1:</b> SEM images of (a) EBL D-05, (b) EBL D-22, (c) EBL D-15 after 30 minutes of growth time in the HFCVD reactor.....	32
<b>Figure 3.2:</b> SEM images of (a) EBL D-22 and (b) EBL D-15 after 55 minutes of growth time in the HFCVD reactor.....	34
<b>Figure 3.3:</b> Laser Raman spectra of EBL D-05 (P600), EBL D-22 (P800), and EBL D-15 (P1000) BDD electrodes using 514 nm laser excitation. Each spectrum has been offset vertically for comparison .....	36
<b>Figure 3.4:</b> CV of EBL BDD samples of the T200 P600 design after different oxygen treatments: O <sub>3</sub> (AOZ); H <sub>2</sub> SO <sub>4</sub> (AOT); and O <sub>2</sub> plasma (AOP) in comparison to a H-terminated electrode of the same design (H-T). ....	37
<b>Figure 3.5:</b> CV of each EBL BDD electrode in background electrolyte 0.1 M KNO <sub>3</sub> , $\nu = 100 \text{ mV s}^{-1}$ .....	39
<b>Figure 3.6:</b> CV of each f-BDD electrode in background electrolyte 0.1 M KNO <sub>3</sub> , $\nu = 100 \text{ mV s}^{-1}$ .....	42
<b>Figure 3.7:</b> CV of f-BDD-01 in comparison to EBL D-05 in background electrolyte 0.1 M KNO <sub>3</sub> , $\nu = 100 \text{ mV s}^{-1}$ .....	43
<b>Figure 3.8:</b> Visual representation of the geometric surface area ( <i>A<sub>g</sub></i> ) and actual surface area ( <i>S<sub>Actual</sub></i> ) of EBL BDD electrodes when in the electrode holder (not to scale).....	47
<b>Figure 3.9:</b> CV of 0.5 M H <sub>2</sub> SO <sub>4</sub> and 0.5 M H <sub>2</sub> SO <sub>4</sub> + 25 mM FF, $\nu = 100 \text{ mV s}^{-1}$ with EBL D-22.....	49



# List of Abbreviations and Symbols

## Abbreviations

<b>AFM</b>	Atomic force microscopy
<b>AOP</b>	O <sub>2</sub> plasma treatment
<b>AOT</b>	H <sub>2</sub> SO <sub>4</sub> treatment
<b>AOZ</b>	Ozone treatment
<b>bD</b>	Black diamond
<b>BDD</b>	Boron-doped diamond
<b>B/C</b>	Boron to carbon ratio
<b>bSi</b>	Black silicon
<b>CB</b>	Conduction band
<b>CNTs</b>	Carbon nanotubes
<b>CV</b>	Cyclic voltammetry
<b>CVD</b>	Chemical vapour deposition
<b>DND</b>	Detonation nanodiamond
<b>EBL</b>	Electron beam lithography
<b>e-beam</b>	Electron beam
<b>EDL</b>	Electrochemical double layer
<b>f-BDD</b>	Flat boron-doped diamond
<b>FCA</b>	Furoic acid
<b>FDCA</b>	Furandicarboxylic acid
<b>FF</b>	Furfural
<b>HER</b>	Hydrogen evolution reaction
<b>HFCVD</b>	Hot filament chemical vapour deposition
<b>HMF</b>	5-hydroxymethylfurfural
<b>HFN</b>	5-hydroxy-2(5 <i>H</i> )-furanone
<b>HPHT</b>	High-pressure high-temperature
<b>ICP</b>	Inductively coupled plasma
<b>IHP</b>	Inner Helmholtz plane
<b>IPA</b>	Isopropanol

<b>LIPSS</b>	Laser-induced periodic surface structuring
<b>LCB</b>	Lignocellulosic biomass
<b>MA</b>	Maleic acid
<b>MIBK:IPA</b>	Methyl isobutyl ketone : isopropanol
<b>MPCVD</b>	Microwave plasma-assisted chemical vapour deposition
<b>MWCNTs</b>	Multi-walled carbon nanotubes
<b>MWCVD</b>	Microwave chemical vapour deposition
<b>NCD</b>	Nanocrystalline diamond
<b>OER</b>	Oxygen evolution reaction
<b>OHP</b>	Outer Helmholtz plane
<b>PMMA</b>	Poly(methyl methacrylate)
<b>PTFE</b>	Polytetrafluoroethylene
<b>RIE</b>	Reactive-ion etching
<b>RF</b>	Radio frequency
<b>SEM</b>	Scanning electron microscopy
<b>SIMS</b>	Secondary ion mass spectroscopy
<b>SWCNTs</b>	Single-walled carbon nanotubes
<b>VACNTs</b>	Vertically aligned carbon nanotubes
<b>VB</b>	Valence band

## Symbols

$A_g$	Geometric surface area	$\text{cm}^2$
$C_{dl}$	Double-layer capacitance	$\mu\text{F cm}^{-2}$
$E_g$	Band gap energy	eV
$i_{av}$	Average current at $V = 0$	A
$S_{\text{actual}}$	Actual surface area	$\text{nm}^2$
$\nu$	Scan rate	$\text{V s}^{-1}$ (for calculations)

# 1. Introduction

## 1.1. Microstructured Electrodes

The term microstructured electrodes encompasses electrodes designed with specific engineered features on the micro- to nanoscale that significantly enhance the physical, chemical, and electrochemical properties of the electrodes. A notable example of successful microstructured electrodes is those based on diamond which uses its unique properties to enhance electrochemical performance, particularly when doped to induce conductivity.

Atomically flat boron-doped diamond electrodes (f-BDD) were among the first substrates used for developing diamond electrodes, and these remain a prominent material choice in electrochemical research and application due to their low background current and wide working potential window.<sup>1</sup> Grown on single-crystal silicon wafers, the f-BDD layer has a flat, uniform topography achieved through post-fabrication polishing. Although numerous applications for f-BDD electrodes have long been identified, achieving optimal efficiency requires strategies to maximise the electrochemically active surface area. One effective approach to this is the miniaturisation of electrode structures to the nanoscale—which is inherently challenging to achieve.<sup>2</sup> An example of this is to combine the desirable qualities of f-BDD and grow boron-doped diamond (BDD) on substrates with large surface areas. This method not only amplifies electrochemical performance across a variety of applications but also introduces the possibilities for harnessing the potential of diamond in electrochemical systems.

## 1.2. Diamond in Electrochemistry

### 1.2.1. Diamond Properties

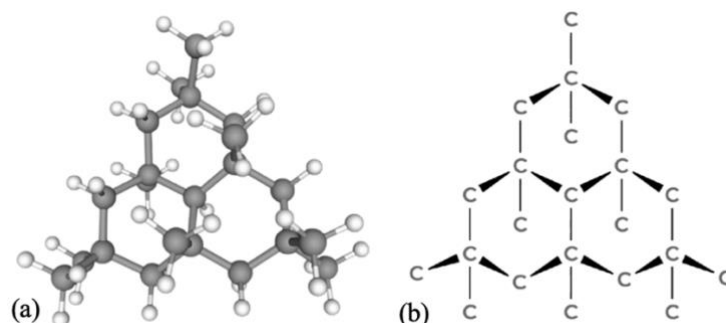


**Figure 1.1:** The structure of diamond in both (a) ball and stick form and (b) chemical structure.

Diamond possesses a tetrahedral symmetry, formed by two interlinked face-centred cubic lattices. (**Fig. 1.1**) Each carbon atom is covalently bonded to four neighbouring carbon atoms, creating a very strong tetrahedral lattice that lacks delocalized  $\pi$ -electrons, which would otherwise increase reactivity.<sup>3</sup> To allow for tetrahedral symmetry, the carbon atoms undergo  $sp^3$  hybridisation, where the 2s electrons are promoted to the 2p orbitals, enabling the formation of strong covalent bonds with bond angles of  $109^\circ$ . Consequently, all carbon atoms in diamond are  $sp^3$  hybridized. The distinction between diamond and graphite lies in the stacking sequence of their atomic layers: cubic diamond follows an ABCABC stacking sequence, whereas hexagonal graphite exhibits an ABABAB stacking arrangement, as illustrated in **Figure 1.2**.<sup>4</sup>

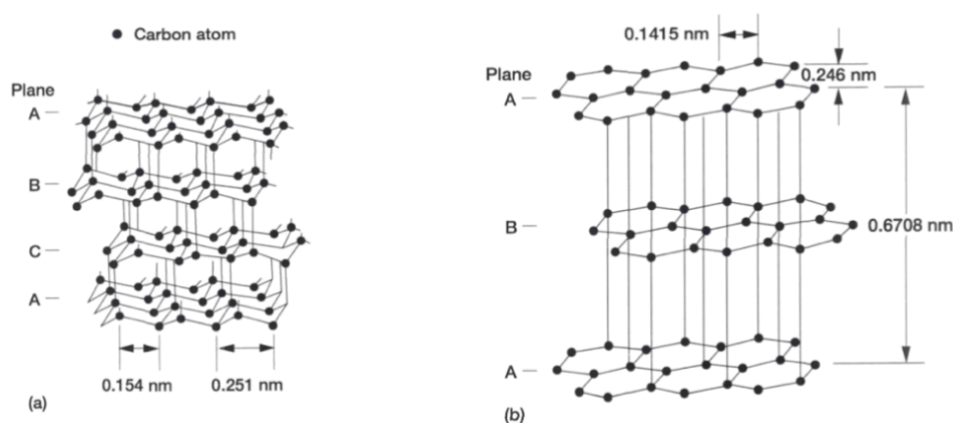


**Figure 1.2:** Schematic diagrams of the crystal structures of cubic symmetry diamond structure (ABCABC) and hexagonal symmetry graphite structure (ABABAB) taken from **Ref. 4**.

In chemical vapour deposition (CVD) diamond, the cubic structure of diamond is the most common form of diamond grown due to its thermodynamic stability and lower energy barriers. The cubic structure can be visualised as infinite layers of the planes with Miller indices  $\{111\}$  and/or  $\{100\}$  seen in **Figure 1.3**.<sup>5</sup> The  $\{111\}$  and  $\{100\}$  facets are the most common among the four low-index crystallographic planes typically observed in synthetically grown diamond under varying conditions.<sup>6-8</sup>

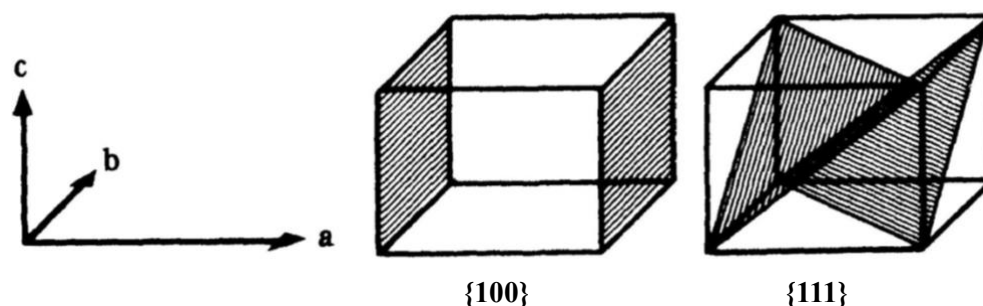


**Figure 1.3:** Simple visualisations of the  $\{100\}$  and  $\{111\}$  planes of crystal diamond taken from **Ref. 5**.

The strong covalent bonds of the diamond structure make it one of the hardest known materials, exhibiting high resistance to abrasion, mechanical degradation, and a high Young's modulus. Additionally, the absence of delocalised  $\pi$ -electrons in its lattice contributes to the diamond's resistance to oxidation and corrosion further enhancing its durability and chemical stability.<sup>9,10</sup> Electrodes with a diamond surface, particularly BDD, exhibit high inertness and smoothness due to fewer surface functional groups, which minimises the likelihood of adsorbance of fouling contaminants. This anti-fouling property contributes to consistent electrochemical performance over time.<sup>11</sup> Due to these properties, the synthetic growth of diamond for use in electrochemical and other appliances has become widely popular.

### 1.2.2. Electrochemical Performance

Diamond's large energy gap between the filled valence and empty conduction bands means that electrons cannot easily be excited into the conduction band. There are also no free charge carriers, electrons or 'holes', to allow for the flow of electric current. Therefore, undoped diamond is considered to be an electrical insulator.<sup>12</sup>

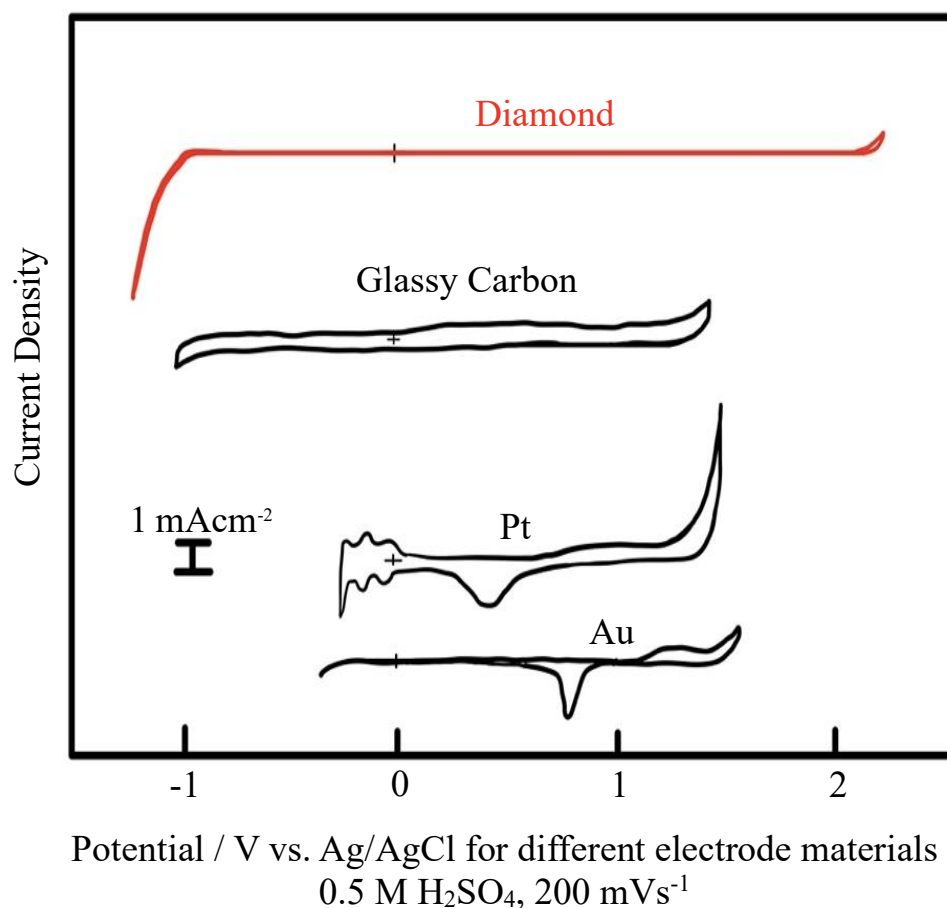


**Figure 1.4:** Potential windows of different common electrodes. Redrawn using data from **Ref. 13**.

The electrochemical potential window is the range of applied potential differences that encompasses the electrochemical redox reactions of interest. For diamond electrodes, this is wider than that of any other material due to its extreme inert nature which minimises unwanted electrochemical reactions at the surface, allowing for a broader range of voltages without suffering significant background current. (**Fig. 1.4**)<sup>13</sup> This window encompasses most electrochemical reactions within the potential range -1 to +1.8 V. Furthermore, diamond electrodes exhibit extremely low background, therefore the baseline signal is very stable across a wide range of potentials.

### 1.2.3. Band Gap Theory

The band gap ( $E_g$ ) of a material pertains to the energy difference between the valence band (VB) and the conduction band (CB). The VB is the highest range of electron energies where electrons are normally present at absolute zero temperature. When electrons are thermally

excited, they move from the VB to the CB. The size of  $E_g$  and the electrons in the CB directly influence a material's electrical conductivity.<sup>14</sup> Conductors, typically metals, have an overlapping or non-existent band gap of  $\approx 0$  eV allowing the free movements of electrons resulting in high electrical conductivity. Semiconductors have a band gap of  $\sim 0.1-3$  eV, small enough that electrons can be thermally or optically excited from the VB to the CB, giving controllable conductivity that can be enhanced by doping. Insulators have a large band gap above 3 eV that prevents electrons from easily promoting to the CB making these materials poor electrical conductors. Intrinsic diamond is an example of an insulator with a wide band gap of  $\sim 5.5$  eV.<sup>15</sup>

#### 1.2.4. Semiconductors

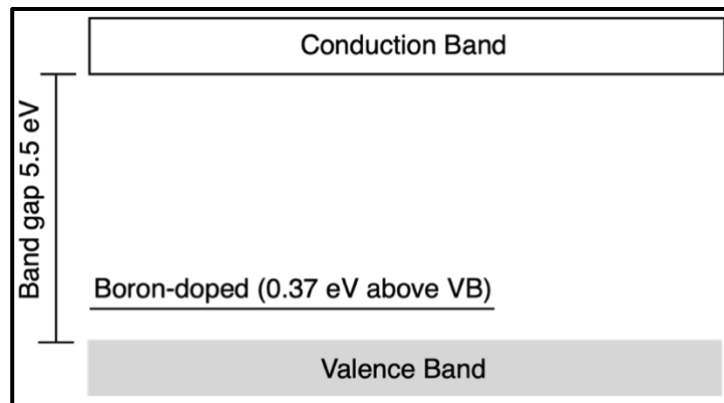


**Figure 1.5:** The effect of B doping on the band gap of diamond. Without the acceptor level, to make diamond conductive electrons would need to be excited from the valence band to the conduction band across 5.5 eV but the acceptor level greatly decreases this gap to only 0.37 eV for electrons to jump and give a conducting material.

Semiconductors specifically are highly tuneable and can be engineered for electronic and electrochemical applications. A common method to modify conductivity is extrinsic doping whereby impurities are intentionally added into electrically active sites within the lattice of a material.<sup>16</sup> Conductivity is enhanced by introducing additional charge carriers that reduce the material's effective band gap. An n-type semiconductor involves doping with elements with extra electrons than the bulk atoms and enhancing conduction via these extra electrons being located in a 'donor' band situated just below the CB. Thus, it takes little energy to excite these electrons from the donor band into the empty CB, from where they can move freely throughout

the material, i.e. electrical conduction. A p-type semiconductor is created by doping with elements that have fewer valence electrons than the bulk atoms, resulting in an empty ‘acceptor band’ located just above the VB. Again, little energy is now needed to excite electrons from the full VB into this acceptor level. Having lost electrons, the VB is now no longer full, and therefore the remaining electrons can now freely move through the VB enabling electrical conduction. In this case, the lack of electrons or ‘holes’ in the VB are considered to be the majority carriers.<sup>17</sup> Boron (B) is the most practical dopant when substituted in diamond to a low concentration. It alters the material’s electronic properties without having significant effect to the structural lattice and performance of the electrodes. The addition of B in place of carbon atoms, forms an impurity level of acceptors with a shallow activation energy of 0.37 eV above the VB as seen in **Figure 1.5**.<sup>18</sup>

Following doping with B, diamond transitions from an insulator to a p-type semiconductor. With very low B doping, the B atoms are quite far apart and can be considered as almost isolated in the lattice. In this case, hopping conduction takes place, where holes are directly transferred between B impurities, bypassing the valence band, and has been observed in literature in both single and polycrystalline diamond films.<sup>19,20</sup> At higher doping levels, the acceptor band covers the entire material, and conduction occurs through the movement of holes in the valence band, and the conduction becomes metallic. Despite the introduction of some p-type conductivity, BDD maintains a wide electrochemical potential window in aqueous solutions, typically ranging from -1.35 V to +2.3 V.<sup>21</sup> This is attributed to the chemical stability of diamond itself.

The introduction of B also alters the morphology of the CVD diamond surface via the individual crystal facets. At lower concentrations the crystal structure exhibits an equal ratio of both {100} and {111} facets. As the B concentration increases to higher ppm levels the {111} facets tend to dominate over the {100} facets.<sup>22</sup> Furthermore, a higher concentration of B typically results in the formation of rougher or rounder diamond crystal facets suggesting a deterioration in crystal morphology. Increased B concentration in the gas phase during CVD also decreases gas-phase H species, therefore etching of sp<sup>2</sup> carbon by H atoms becomes less effective, leading to higher sp<sup>2</sup> defects on the diamond surface, particularly at grain boundaries. Subsequently, a doping limit has been suggested of ~30,000 ppm B/C ratio before B begins to diminish diamond quality.<sup>23</sup>

### 1.3. Fabrication Approaches for High Surface Area BDD Electrodes

The current fabrication of nanostructured BDD electrodes with large surface areas can be broadly classified into two approaches: top-down etching and bottom-up growth.<sup>24</sup> Top-down processing involves the etching of the diamond layer while bottom-up processing involves direct growth of diamond layers onto pre-structured substrates.

#### 1.3.1. Top-Down Etching

##### Reactive Ion Etching

Reactive ion etching (RIE) is an advanced technique pioneered by Hosokawa et al. that utilises capacitively or inductively plasmas to etch the surface of a substrate.<sup>25</sup> Ions are accelerated by the electric field within the plasma, driving them to collide with the substrate and remove surface material. By combining chemical and physical etching mechanisms, RIE allows for the precise removal of material layers, enabling intricate nanostructured patterns on the substrate. The patterns are formed through the use of a mask which serves as a physical barrier to ensure only exposed regions of the substrate are etched away by the reactive plasma. The use of RIE with diamond began with using a  $\text{CF}_4/\text{O}_2$  plasma, enabling the formation of porous diamond films.<sup>26</sup> Further development introduced metal nanoparticles such as Ni acting as micro-masks to form nanopillars/wires.<sup>27</sup> In studies involving BDD films, a boron-doped oxygen plasma was used to fabricate spiked structures onto the film surface.<sup>28</sup>

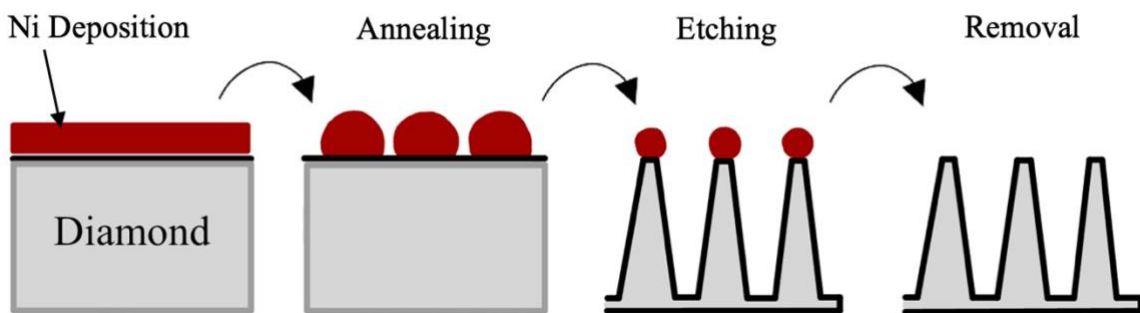


**Figure 1.6:** Mechanism for the fabrication of diamond nanowires from Ni nanoparticles using RIE redrawn from **Ref. 29**.

## Nanowires

Diamond nanowires can be fabricated by a top-down approach involving f-BDD substrates and an etching mask from metal, boron or nanodiamond particles deposited onto the substrate surface, as demonstrated by Nebel et al.<sup>29</sup>, (**Fig. 1.6**). The nanowires are generated by the reduction of large systems to a small size usually through the use of RIE. An example of vertically aligned diamond nanowires synthesised using nanodiamond particles as masks can be seen in **Figure 1.7**.<sup>28</sup> Recent developments of nanowires on free-standing BDD film offer a solution to the damage caused by the RIE process leading to loss of adhesion of the film and substrate.<sup>30</sup> RIE involves bombarding the substrate with energetic ions which can lead to mechanical stress and erode material at the interface which reduces contact and adhesion. The development of nanowires on free-standing BDD film provide a more stable structural approach that minimises adhesion loss by creating a more mechanically flexible structure that distributes mechanical forces more effectively and provide stronger anchoring points for the film.

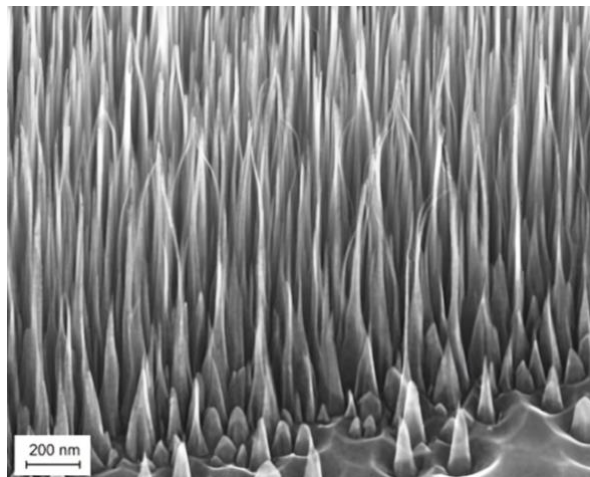


**Figure 1.7:** SEM image of vertically aligned BDD nanowires using diamond nanoparticles as masks taken from **Ref. 28**.

## VACNTs

Vertically aligned carbon nanotubes (VACNTs) are arrays or “forests” of carbon nanotubes (CNTs) grown to stand perpendicular to a substrate surface. The CNTs can be single-walled (SWCNTs) or multi-walled (MWCNTs). Zou et al. developed the “forest” technique resulting in ‘tepee’ structures from electrospray deposition seeding of nanocrystalline BDD for field

emission purposes, (**Fig. 1.8**).<sup>31</sup> This technique is often favoured over SWCNTs for their enhanced strength, resilience, and durability. Their layered structure provides greater mechanical robustness and thermal stability for applications requiring high resistance to formation. In electrochemical applications, the VACNTs have surface areas 450 times greater than flat diamond and a capacitance of between 150-450 times greater than flat diamond counterparts.<sup>32</sup>

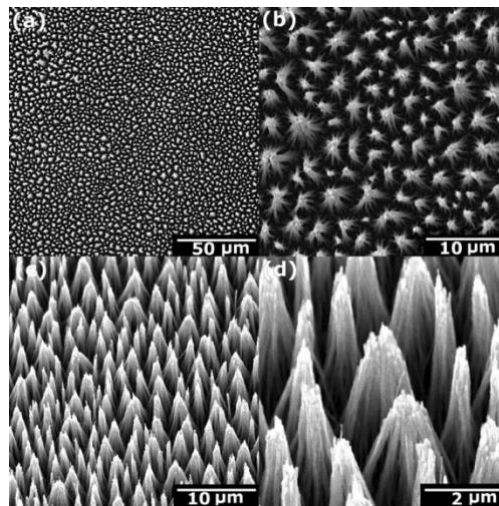


**Figure 1.8:** Top view (a) and (b) and tilt-view (c) and (d) SEM images of VACNT forests taken from **Ref. 31**

However, VACNTs are prone to oxidation or degradation under harsh electrochemical conditions particularly when using high electrochemical potentials. Furthermore, achieving a uniform and adherent diamond layer on these structures is technically challenging due to the alignment and nanoscale dimensions of the VACNT forests.

### **Black Silicon**

Black silicon (bSi) is a nanostructured form of silicon wafers that have been engineered via a RIE technique to possess an enhanced surface area due to nanoscale features such as needles, cones or spike-shaped structures. As a result of the nanoscale features, the wafers appear black.<sup>33</sup> The use of RIE to engineer the spikes of bSi surface was first introduced by Jansen et al.<sup>34</sup> and involves the use of micro masks to etch the silicon wafer into thin needles as seen in **Figure 1.9**. The density of the silicon needles can be controlled by factors such as the composition of the gas phase and the temperature at which they are engineered.

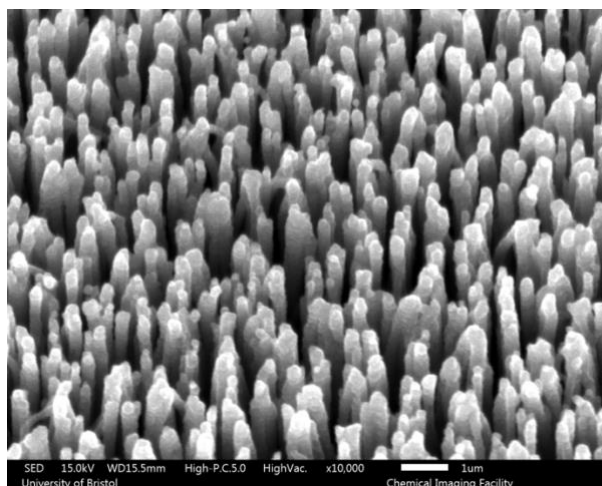


**Figure 1.9:** SEM image of bSi columns after a coating of BDD.

The resulting bSi substrates are coated with BDD by a selected CVD technique and produce uniform ‘black diamond’ (BD) electrodes with a relative effective surface area of approximately 97 times greater than that of f-BDD electrodes and a double-layer capacitance of approximately 50 times that of f-BDD electrodes.<sup>35</sup>

### **Electron Beam Lithography**

Further high-resolution techniques have been developed to increase the surface area of substrates for diamond deposition. Electron beam lithography (EBL) is an innovation created to produce surface patterns at the nanoscale through the modification of scanning electron microscope (SEM) technology.<sup>36</sup> EBL for the specific application of high-performance diamond electrodes is part of new advances in combining nanotechnology and lithographic methods for electrode design. The technique employs a finely focused Gaussian electron beam (e-beam) to etch pre-determined patterns directly onto a substrate with high precision through several critical steps. The substrate - typically a Si wafer - is spin-coated with a thin film of electron-sensitive resist. The e-beam is directed across the resist-coated substrate under vacuum to reduce gas scattering. The e-beam interacts with the resist, altering its physical or chemical properties to create a latent image where exposed areas become chemically or structurally different from unexposed ones. These alterations change the solubility of the resist: in a positive resist, exposed regions become more soluble, while in a negative resist, unexposed regions become less soluble in the developer solution. During development, the solvent selectively dissolves the exposed patterned fragments (positive-tone resist) or unexposed

remaining areas (negative-tone resist). This creates a patterned layer of resist on the surface. A metal layer is deposited onto the substrate, and during the lift-off process both the resist layer and excess metal are then removed through a lift-off process using a chemical wash or burnt off using a plasma ‘ash’ process. The desired pattern is then transferred into the substrate by an anisotropic etching process, typically RIE.<sup>37</sup>

In terms of top-down approaches, the combination of EBL and RIE has become a leading technique for achieving high-resolution patterning in recent years.<sup>38</sup> For nanostructuring Si substrates prior to the deposition of BDD films, RIE in combination with EBL typically employs fluorine-based gases such as SF<sub>6</sub> and CHF<sub>3</sub>, which generate reactive fluorine species that form volatile silicon fluorides for efficient material removal. In addition, inert gases such as Ar are often incorporated to enhance physical sputtering effects and improve etch profile anisotropy.<sup>39,40</sup> However, production of EBL samples can have high operating costs and low processing times that necessitate a very stable environment.<sup>41</sup> Nevertheless, it remains a highly precise nanofabrication method, particularly for creating uniform nanoscale columns to enhance surface area.

### 1.3.2. Bottom-up growth

#### **Seeding**

The seeding of a substrate for diamond deposition enhances nucleation density and ensures uniform diamond growth on the substrate. Studies indicate that a higher seed density accelerates the coalescence of the diamond film.<sup>42</sup> Seeding involves the deposition of nanoparticles of diamond onto a substrate, which serve as seed crystals for future diamond growth.<sup>43</sup> Different seeding techniques are currently utilised in the process of diamond fabrication. One method, mechanical abrasion, involves polishing the substrate with nanodiamond particles to form surface defects, a process first introduced in the 1980s.<sup>44</sup> A key advantage of this method is its simplicity and cost-effectiveness. Another technique is ultrasonic abrasion, whereby the chosen substrate is immersed in a colloidal suspension of nanodiamond particles and subjected to ultrasonication to disperse the nanodiamond particles uniformly across the substrate surface.<sup>45</sup> The primary benefit here is the ability to achieve

uniform seeding density, which is essential for high-quality diamond film growth. Both methods optimise diamond nucleation for multiple applications.

## Electrospray

For nanocrystalline diamond (NCD), such as the diamond grown on EBL Si, abrasion techniques can be too aggressive for the extremely small diamond grains. Therefore, the electrospray seeding method is more appropriate. This method operates by applying a significant potential difference between the grounded substrate and suspension of a nanoparticle (in this case nanodiamond) in a volatile liquid, e.g. water or methanol. Due to the potential difference, the suspension experiences a strong electrostatic force, which causes it to vaporise into droplets and rapidly accelerate in the direction of the substrate.<sup>46</sup> The droplets deposit onto the substrate surface without causing surface damage, and evaporate, leaving the nanodiamond particles behind. This approach ensures a high nucleation density, even over complex 3D topography such as needles, creating an optimal foundation for subsequent diamond film deposition through CVD.<sup>47</sup>

## 1.4. CVD: Chemical Vapour Deposition

The fabrication of diamond electrodes has been made possible by the development of diamond CVD.<sup>48</sup> The CVD process was first patented by William G. Eversole in 1962 for the growth of diamond on seed crystals.<sup>49</sup> The described deposition takes place as:



The reason for favoured diamond deposition (**eqn (1.1)**) over graphite (**eqn (1.2)**) is the specific pressure conditions where diamond is metastable with respect to graphite. The CVD method was developed by Eversole to include hydrogen in order to preferentially remove graphitic ( $\text{sp}^2$ ) carbon during diamond deposition, preventing graphite co-deposition. However, the diamond growth rates achieved in these early experiments were extremely low and unsuitable for industrial applications. Subsequent advancements, including the effective generation and

use of atomic hydrogen in the deposition process, significantly increased growth rates and enabled the use of a wider variety of substrate materials.

A deposition model for the CVD process for diamond growth begins with the activation of the diamond surface. This activation is facilitated by the removal of surface-bonded hydrogen by atomic hydrogen generated *in situ* through the dissociation of molecular hydrogen. Dissociation of precursor gases CH<sub>4</sub> and H<sub>2</sub> is activated by an energy source such as heat or reactive plasma methods generating reactive species of atomic hydrogen, methyl radicals and hydrocarbons. Dissociation of H<sub>2</sub> is seen in **Figure 1.10a**.



**Figure 1.10a:** Mechanism for the dissociation of H<sub>2</sub> gas *in situ*.

This forms surface carbon radicals that serve as the foundational sites for subsequent carbon addition, (**Fig. 1.10b**).

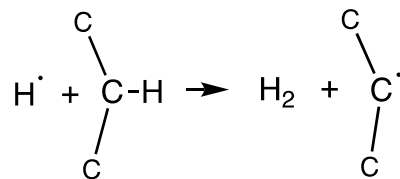


**Figure 1.10b:** Mechanism for the removal of hydrogen from surface carbon.

Also, in the gas phase, H atoms abstract H from methane to produce methyl radicals, CH<sub>3</sub>. The hydrocarbons are dissociated into smaller reactive species such as acetylene or methyl radicals which chemically bond to the exposed carbon radicals contributing carbon atoms for the formation of the diamond film, (**Fig. 1.10c**).

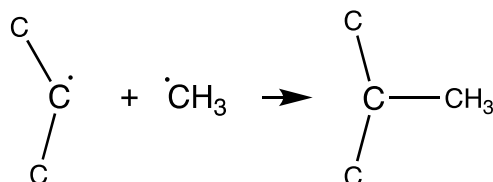


**Figure 1.10c:** Mechanism for the addition of methyl radical to activated surface carbon radical.<sup>50,51</sup>

Diamond crystals grow in specific orientations of close-packed layers (e.g. {111} or {100} planes) dependent on substrate material and growth conditions. Carbon atoms continue to bond to existing diamond lattice sites and thereby a thin diamond film is formed on top of the

substrate. Research has established  $\text{CH}_3$  radicals serve as the primary precursors for diamond film growth and therefore the growth process is highly reliant on methane concentration.<sup>52,53</sup>

#### 1.4.1. Chemical Vapour Mixture

The CVD technique focuses on the two principal discoveries that diamond could be grown beyond its range of thermodynamic stability and that hydrogen is critical to the consistent inhibition of permanent graphite nucleation and removal of non-diamond carbon.<sup>54</sup> Research into the use of atomic hydrogen in the gas mixture during growth was first published by Fedoseev et al. from work initiated by Valentin Varnin.<sup>55</sup> During diamond growth from carbon, atomic hydrogen plays a crucial role by selectively etching away graphite from the deposited carbon. This process occurs as atomic hydrogen is generated near the surface of the growing film, ensuring the formation of high-purity diamond.<sup>56</sup> Atomic hydrogen also stabilises residual  $\text{sp}^3$  bonds on the diamond surface, facilitating orderly, layer-by-layer growth. Without this stabilisation, the diamond surface would revert to the graphite structure.<sup>57</sup>

Many CVD processes use a  $\text{CH}_4/\text{H}_2$  source gas mixture for the production of diamond films with a 100:1  $\text{H}_2$ -to- $\text{CH}_4$  ratio.<sup>58,59</sup> When boron is introduced into the gas mixture in the form of  $\text{B}_2\text{H}_6$  as a dopant, various boron-containing species ( $\text{BH}_x$ ,  $x = 0-2$ ), are generated. These species incorporate into the growing diamond film either through a low energy  $\text{BH}_{x+1}$  intermediate or via direct abstraction, both facilitated by atomic hydrogen.<sup>60</sup>

#### 1.4.2. Microwave Plasma-Enhanced Chemical Vapour Deposition

Microwave plasma-enhanced chemical vapour deposition (MWCVD) is a specialised technique used to deposit thin films of diamond onto substrates. It uses microwave energy (excitation frequency 2.45 GHz) to generate a high-density plasma ball above a desired substrate. The plasma dissociates molecular hydrogen into atomic hydrogen and simultaneously activates hydrocarbon species leading to diamond deposition.<sup>61</sup> Microwaves are introduced to the reaction chamber through a specialised quartz window, which acts as a transparent medium for the electromagnetic waves. These microwaves transmit energy to the gas mixtures, ionising the gases and igniting the plasma. As the microwave power increases, the size of the plasma ball expands, and the temperature on the substrate surface also rises.<sup>62</sup>

The concept was initially demonstrated by Kamo et al at NIRIM in Japan with the NIRIM-type reactor.<sup>63</sup> Since then, it has undergone advancements as illustrated in **Figure 1.11**, which depicts a schematic of an ASTeX-type CVD reactor.<sup>64</sup> It was developed by Bachmann et al. to give the resulting apparatus.<sup>65</sup> This design addressed and resolved many of the limitations prevalent in the NIRIM design.<sup>66</sup>

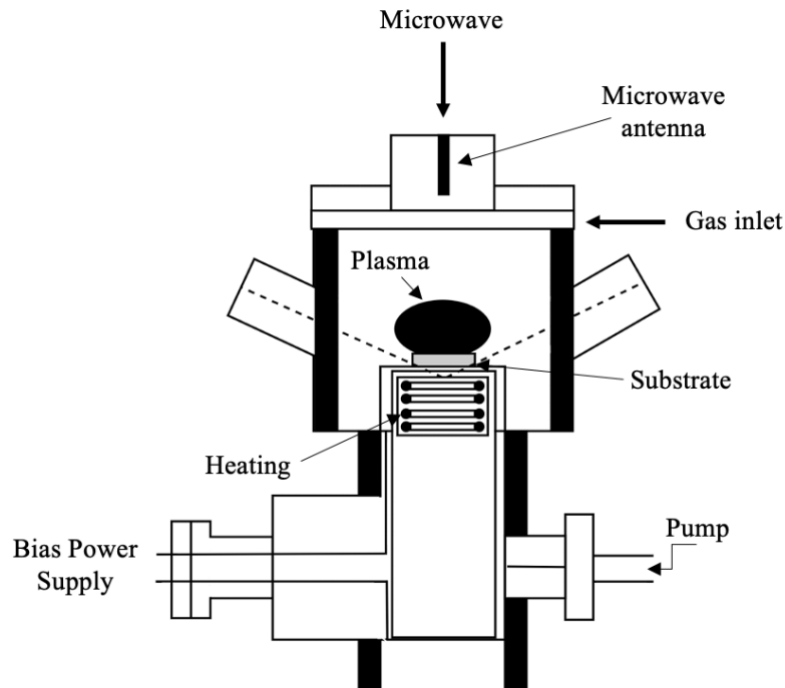


**Figure 1.11:** Schematic diagram of a MWCVD setup taken from **Ref. 65**.

However, there are a couple of major drawbacks to the MWCVD technique. First, the restrictions on substrate size by the plasma size. Scaling up to cover large substrates is possible but challenging and can lead to non-uniform deposition or require high microwave power.<sup>67</sup> Secondly, at higher plasma power levels the plasma tends to become unstable, and the quartz window may be damaged.

### 1.4.3. Hot Filament Chemical Vapour Deposition

Hot filament chemical vapour deposition (HFCVD) is a technique involving a refractory metal filament, typically of tungsten or tantalum, heated to a temperature  $> 2000^{\circ}\text{C}$  above a chosen substrate. The hot filament fragments the gas mixture of methane and hydrogen to deposit a diamond film onto the surface of the substrate. The substrate itself is heated from above by radiant heat from the filament and a separate heater below which allows the substrate to be

maintained at a controlled temperature. The specific technique was first fabricated by Matsumoto et al.<sup>68</sup> and developed upon preceding vapour deposition apparatuses from 1969 proposed by McNeilly and Benzing and Chauhan et al.<sup>69–71</sup> HFCVD is one of the most common methods of diamond nucleation due to its comparative ease and inexpensive equipment. A schematic diagram of the equipment set up for HFCVD can be seen in **Figure 1.12**.<sup>72</sup>

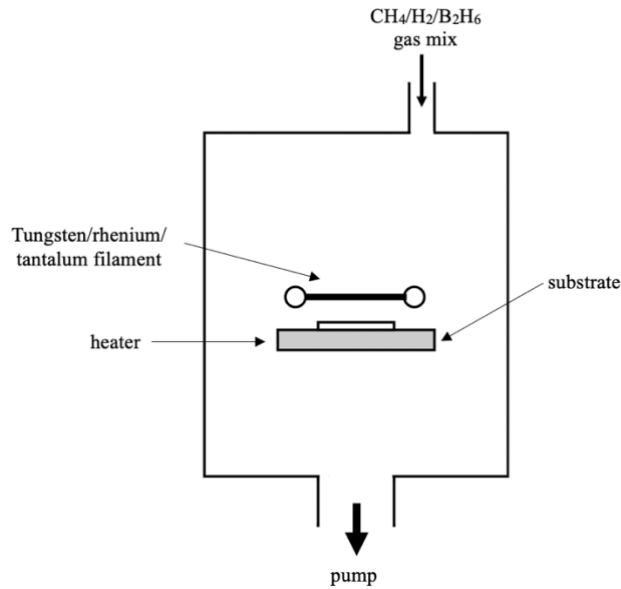


**Figure 1.12:** Schematic diagram of a HFCVD set up taken from **Ref. 72**.

HFCVD allows precise control over the deposition process, resulting in high-quality, single or polycrystalline diamond films with low defect density. Subsequently, HFCVD has been seen to produce conformal and uniform coatings of diamond on multiple different substrates with high surface areas, high capacitance values and high stability.<sup>73,74</sup> It is particularly effective for introducing dopants such as boron to produce doped diamond electrodes that are electrically semiconductive. However, diamond growth via HFCVD is relatively slow, ranging from 0.2 to 1.0  $\mu\text{m/h}$ .<sup>75</sup> Studies have shown that increasing the temperature of a Ta filament to 3000 °C in a CH<sub>4</sub>/H<sub>2</sub> (5%) gas mixture can achieve significantly higher growth rates of up to 17.9  $\mu\text{m/h}$ .<sup>76</sup> Nonetheless, in terms of industrial applications, MWCVD or high-pressure high-temperature (HPHT) methods with faster growth rates are generally preferred.

## 1.5. Electrode Characterisation and Analysis

### 1.5.1. Scanning Electron Microscopy

SEM is a powerful imaging technique used for very high-resolution study of the surface structure, composition, and morphology of materials. It works on a nanometre to micrometre scale to produce images at 300,000 – 500,000 $\times$  magnification.<sup>77, 78</sup> In the context of micro- and nanostructured diamond electrodes, it can be used to visualise the specific structure of the substrate before and after diamond deposition through micrographs to ensure successful diamond film formation and uniformity.

### 1.5.2. Laser Raman Spectroscopy

Laser Raman spectroscopy is an analytical technique that provides information about the molecular structure, chemical composition, and phase of a sample. This non-destructive technique requires minimal to no preparation and places few restrictions on the sample size. It utilises inelastic scattering of photons to analyse the vibrational modes of molecules or materials. Raman spectroscopy is especially advantageous for samples involving carbon, due to its capability to differentiate between carbon allotropes, each of which exhibits a unique Raman signature. The Raman spectrum of pure diamond ( $sp^3$  carbon  $\sigma$  bonds only) features a characteristic line at 1332.5  $cm^{-1}$ , corresponding to the vibrational modes of the two interpenetrating cubic sublattices.<sup>79</sup> A higher number of defects leads to a shorter phonon lifetime and a broader line width. As the boron concentration in the diamond matrix increases, the diamond  $sp^3$  peak shifts towards lower wavenumbers and broadens.

Non-carbon diamond ( $sp^2$ ) gives rise to G and D peaks, corresponding to ordered and disorder  $sp^2$  carbon, respectively. In crystalline graphite, the G peak, which signifies an ordered structure, appears at 1575  $cm^{-1}$ , while the D peak, associated with disorder, is observed at 1355  $cm^{-1}$ .<sup>80</sup> When the crystallite size is reduced to the nanoscale, the matrix becomes increasingly disordered. A prominent peak at 1150  $cm^{-1}$  is frequently observed in CVD-synthesised NCD films and is considered to originate from  $sp^2$ -hybridised *trans*-polyacetylene-like structures located at grain boundaries and interfaces.<sup>81</sup>

### 1.5.3. Electrical Conductivity

The electrical conductivity of a film indicates how easily free charge carriers can move through a material under an electrical field. Assessing the electrical conductivity of diamond provides insights into the influence of boron doping to a semiconductor. This analysis helps determine whether the resulting film is an n-type or p-type semiconductor.

### 1.5.4. Double Layer Capacitance

Carbon-based materials, such as diamond, store energy through non-Faradaic charge separation at the electrode-electrolyte boundary. This process is achieved by physical adsorption of ions onto the electrode surface, leading to the formation of an electrical double layer (EDL). Consequently, the electrochemical double layer capacitance ( $C_{dl}$ ) arises as a result of this interfacial charge accumulation. Therefore,  $C_{dl}$  is a non-Faradaic process, and values are the current response purely due to capacitive charging and not from oxidation or reduction reactions. The EDL consists of two parallel layers of positive and negative charge, one on the metal electrode surface and one dispersed in the solution. (Fig. 1.13)

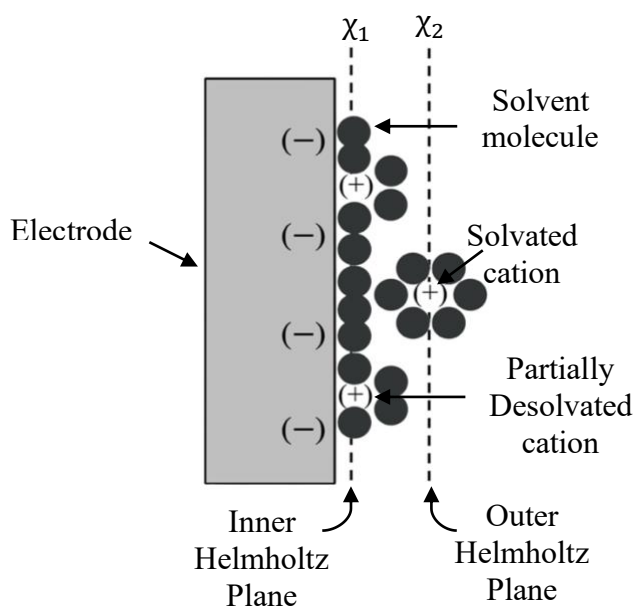


**Figure 1.13:** The electrical double layer drawn with information from Ref. 82. (pg. 13)

The first layer consists of molecules adsorbed to the electrode surface and is known as the inner Helmholtz plane (IHP). The second layer comprises solvated ions and is known as the outer Helmholtz plane (OHP).<sup>82</sup> Ions that remain solvated may only approach as close as the OHP. The solvation layers of the adsorbed ions, however, can create a barrier that interferes with further ion adsorption and charge transfer. The effect is more pronounced in electrodes on the micro- and nanoscale, as the high surface area enables a greater density of adsorbed species. At higher external potentials the barrier layer can become more prominent resulting in a non-linear increase in capacitance.<sup>83,84</sup>

The  $C_{dl}$  is influenced by the real (effective) surface area of the electrode, as increased surface roughness and porosity provide a larger area for charge accumulation, resulting in a higher  $C_{dl}$  value. This capacitance arises purely from electrochemical double-layer charging (capacitive current). This is particularly significant in electrochemical systems, such as sensing, where a larger  $C_{dl}$  improves sensitivity by increasing the interfacial area available for charge separation. While  $C_{dl}$  is physically governed by the real (effective) surface area, it is conventionally reported normalised to the geometric surface area ( $A_g$ ) of the electrode, which represents the projected, two-dimensional area without accounting for surface roughness or porosity.  $C_{dl}$  is typically expressed in units of  $\mu\text{F cm}^{-2}$  and is determined using the average capacitive current ( $i_{av}$  in A) at  $V = 0$ , the scan rate ( $v$  in  $\text{V s}^{-1}$ ) and  $A_g$  (in  $\text{cm}^2$ ), as shown in **eqn (1.3)**, in conjunction with cyclic voltammetry (CV) measurements.

$$C_{dl} = \frac{i_{av}}{vA_g} \quad (1.3)$$

Surface termination plays a crucial role in enhancing the  $C_{dl}$  of CVD diamond electrodes. Hydrogen-terminated electrode surfaces typically exhibit lower capacitance due to their hydrophobic nature and limited ion adsorption. Oxygen-terminated surfaces have increased surface polarity and therefore increased  $C_{dl}$ . Specific functionalisation enhances the electrode electrochemical performance by at least 9 times.<sup>85</sup> Gas-phase methods such as  $\text{O}_2$  plasma treatment, ozone treatment in air by ultraviolet light irradiation, and liquid-phase methods such as thermal treatment in strong acid and electrochemical oxidation, are commonly used for oxygen termination of electrodes produced

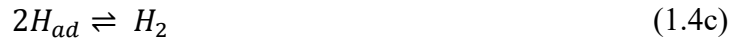
by CVD.<sup>86-89</sup> O<sub>2</sub> plasma treatment can terminate surfaces in very short periods between 1 and 60 seconds without significant effect upon surface morphology.<sup>86</sup> Ozone treatment offers gentle, controlled and uniform oxygen termination for delicate electrode structures.<sup>87</sup> Strong acid treatment is frequently used for complex structures since it is liquid phase and therefore is more likely to modify the entire surface area of the electrode maximising hydrophilicity. It is a low-cost procedure that can also remove resist residues left over from CVD coating.<sup>88</sup>

The  $C_{dl}$  of f-BDD has been observed to range from 2.9  $\mu\text{F cm}^{-2}$  (single-crystal) to 10  $\mu\text{F cm}^{-2}$  (polycrystalline).<sup>35,90</sup> In contrast, micro- and nanostructured carbon-based electrodes exhibit higher  $C_{dl}$  due to the increased electrochemically active surface area.<sup>91-93</sup> Given its direct correlation with electrode surface area and interfacial charge storage, measuring and optimising  $C_{dl}$  is essential for advancing high-performance electrochemical devices based on nanostructured diamond materials. In micro/nanostructured electrodes, capacitance influences impedance and noise levels. Excessive capacitance can lead to sluggish response times, while small capacitances can reduce signal strength.<sup>94</sup> Achieving an optimal balance is crucial for designing high-performance electrodes for electrochemical applications.

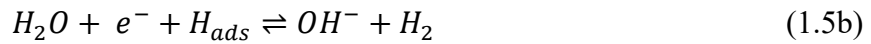
## 1.6. EBL-BDD Electrode Applications

### 1.6.1. The Water Hydrolysis Reaction

Global demand for a reliable and environmentally conscious fuel source is rapidly increasing with population growth and efforts to reduce CO<sub>2</sub> emissions in alignment with the Paris Agreement.<sup>95</sup> The electrochemical splitting of water, or water hydrolysis reaction, represents a fundamental process in the development of sustainable hydrogen energy sources through the conversion of water into H<sub>2</sub> and O<sub>2</sub> gas via the hydrogen evolution reaction (HER) and oxygen evolution reaction (OER) respectively. The HER produces hydrogen gas at the cathode via a sequence of possible steps, which differ depending on the electrolyte. In acidic media, there are two possible reaction steps: the Volmer step (**eqn (1.4a)**) followed by either the Heyrovksy step, involving electrochemical desorption (**eqn (1.4b)**), or the Tafel step, involving chemical recombination (**eqn (1.4c)**), to produce hydrogen gas.<sup>96</sup>



In alkaline media, there are two possible slightly modified reaction steps due to the lower availability of protons. The Volmer step which now involves water molecule dissociation (**eqn (1.5a)**) followed by the Heyrovsky step to generate hydrogen gas and hydroxide ions (**eqn (1.5b)**) or followed by the chemical Tafel step as shown in **eqn (1.4c)**.<sup>97</sup>



Both the HER and OER require highly robust and efficient electrode materials to overcome kinetic barriers and ensure long-term operational stability.<sup>98</sup> BDD has attracted considerable attention due to the unique electrochemical properties detailed in **Section 1.2** – most notably, the exceptionally wide potential window which allows for HER and OER operated at elevated voltages, accommodating the associated high overpotentials but without compromising electrode stability.<sup>99</sup> However despite these advantages, its intrinsic catalytic activity towards the water hydrolysis reaction remains relatively low due to its inert nature. The addition of metal oxide nanoparticles introduces active catalytic centres that facilitate charge transfer at the electrode-electrolyte interface. Incorporating both CuO and ZnO nanoparticles onto BDD electrodes has demonstrated notable improvements concerning the HER and OER, significantly reducing the required overpotentials and therefore energy losses.<sup>100</sup> This enhancement highlights the potential of surface-modified BDD electrodes for sustainable hydrogen production, addressing the growing need for efficient and cost-effective water hydrolysis technologies. Moreover, nanostructuring the BDD electrodes provides an effective approach to further reduce operational costs. By increasing the electrochemically active surface area, nanostructured BDD electrodes can achieve higher catalytic efficiency for more economically viable hydrogen production.

## 1.6.2. Furfural Oxidation

Furfural (FF) is a valuable chemical feedstock of furan derivatives, currently generated in a large abundance. As of 2021, the global annual FF production was estimated over 300 kilotons, with China accounting for approximately 70% of the total output.<sup>101</sup> FF is produced through the acid hydrolysis of hemicellulose-rich biomass residues, in which mineral acids such as HCl or H<sub>2</sub>SO<sub>4</sub> catalyse the depolymerisation of pentosans present in lignocellulosic biomass (LCB) into pentose sugars. These sugars then undergo acid-catalysed dehydration to yield FF.<sup>102</sup> This LCB is globally available in large quantities and serves as a sustainable biofuel alternative.<sup>103,104</sup> Biomass valorisation presents a viable strategy to reduce dependence on fossil fuels for production of chemicals and materials. Transforming substances such as FF into useful products is crucial for sustaining environmental longevity. The presence of an aldehyde functional group in FF enables its further valorisation into higher-value chemicals via sustainable pathways such as oxidation reactions. The oxidation of FF leads to the major products furoic acid (FCA), maleic acid (MA), 5-hydroxy-2(5*H*)-furanone (HFN), and furandicarboxylic acid (FDCA), all of which are value-added chemicals (**Fig. 1.14**).<sup>105</sup> FCA has many applications including its use as another sustainable precursor for bio-based polymers.<sup>106</sup> Maleic acid is a similarly important intermediate for the various industrial products of surface resins and pharmaceuticals.<sup>107,108</sup> HFN has demonstrated potential as a versatile intermediate in the synthesis of both pharmaceutical and agrochemical compounds.<sup>109,110</sup> Finally, while FDCA is predominantly synthesised from 5-hydroxymethylfurfural (HMF) the route via FF presents a significantly more cost-effective and sustainable alternative for commercial-scale production.<sup>111</sup> This is primarily due to FF's large production volumes from LCB which are abundant and inexpensive feedstocks. In contrast, HMF requires more refined carbohydrate sources. Various approaches have been explored with most starting with the relatively simple oxidation of FF to 2-furoic acid offering an easier pathway than that of HMF.<sup>112–114</sup>

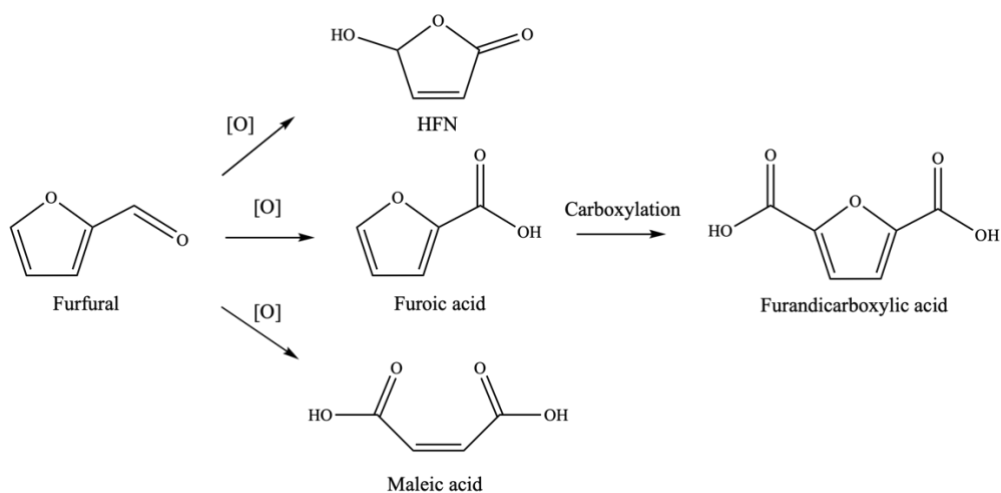


**Figure 1.14:** Furfural oxidation to furoic acid (FCA), maleic acid (MA), 5-hydroxy-2(5*H*)-furanone (HFN), and furandicarboxylic acid (FDCA). Redrawn from information in **Ref. 105**.

Oxidation of FF electrochemically offers a sustainable and energy-efficient alternative to conventional thermal oxidation methods, which typically require high temperatures and pressures.<sup>115</sup> In contrast, electrochemical oxidation operates under milder conditions and allows for direct utilisation of renewable electricity.<sup>116</sup> Given that the oxidation of FF is a surface-dependent process, utilising large surface area BDD electrodes enhances the number of available active sites for FF adsorption and subsequent oxidation reactions. Furthermore, the inherent chemical stability and wide potential window of BDD electrodes makes them ideally suited for operation in alkaline media, while their excellent resistance to corrosion and oxidative degradation ensures chemical stability in acidic media.

### 1.6.3. Electrochemical Sensing

Besides generating fossil fuel alternatives, BDD electrodes have emerged as highly promising materials for electrochemical sensing applications, owing to their unique combination of electrochemical properties. Particularly, the remarkable mechanical and chemical stability of BDD enables sensitive and selective detection of a broad range of analytes under harsh conditions, including extreme pH environments and high anodic potentials.<sup>117,118</sup> Furthermore, the wide potential window of BDD electrodes allows for the detection of heavy metals, pharmaceutical compounds, and neurotransmitters in aqueous environments. For heavy metals

such as Pb, Ni, Cd, and Hg, BDD electrodes facilitate efficient anodic stripping voltammetry, owing to the low background currents and ability to operate at high anodic potentials of BDD without interference from water oxidation.<sup>119,120</sup> Similarly, BDD electrodes have proven effective in the electrochemical detection of pharmaceuticals, including antibiotics and non-steroidal anti-inflammatory drugs, as their oxidation typically necessitates high overpotentials when using conventional electrodes.<sup>121,122</sup> Moreover, the detection of biologically relevant neurotransmitters namely dopamine, serotonin, and epinephrine benefits significantly from the stable electrochemical behaviour of BDD which minimises electrode fouling.<sup>123–125</sup> This allows for distinct peak separation even in complex aqueous matrices.

## 1.7. Scope of the Project

This project aims to optimise the surface area of boron-doped nanocrystalline diamond electrodes to achieve a high double-layer capacitance for optimised electrochemical performance, while maintain fast electrode response times essential for practical applications. The primary objective will be to develop high surface area electrode through a combination of top-down etching and bottom-up growth techniques mentioned in this section – namely, RIE and EBL to define nanoscale features, followed by HFCVD to grow conformal BDD films. By employing these complementary techniques, the study aims to increase the geometric surface area of BDD electrodes, thereby improving their capacitance, charge store capabilities, and overall electrochemical efficiency.

Three distinct EBL-BDD electrode designs will be fabricated to investigate the relationship between surface morphology and electrochemical performance. Following fabrication, the electrodes will be characterised and subsequently tested electrochemically by measuring double-layer capacitance ( $C_{dl}$ ) in  $\text{KNO}_3$  solution at a scan rate of  $100 \text{ mV s}^{-1}$  over a potential range of  $-0.1 \text{ V}$  to  $0.1 \text{ V}$  (vs. Ag/AgCl). The results will provide critical insights into the effectiveness of the nanostructuring approach for measurable improvements in capacitive behaviour. In addition to baseline electrochemical characterisation, the study will explore the development of the application potential of the newly grown high surface area BDD electrodes for the electrochemical oxidation of FF, a key biomass-derived platform chemical. Preliminary FF oxidation experiments will be conducted in acidic media to assess oxidative activity of the EBL-BDD electrodes, with the objective of generating valuable products such as furoic acid

and maleic acid. Although these initial trials will be performed without the inclusion of additional catalytic specific, they will serve to evaluate the intrinsic activity of the BDD surface.

## 2. Experimental

### 2.1. EBL-Si Substrate Preparation

The Si substrates were prepared from 100 mm diameter, highly conductive p-type B-doped {100} oriented Si wafers, with a thickness of 500  $\mu\text{m}$  and an electrical resistivity range of 0.001-0.005  $\Omega\cdot\text{cm}$ . These wafers were sectioned into  $10 \times 10$  mm samples using an *Oxford Lasers* laser cutting system. Following cutting, the samples were cleaned with isopropanol (IPA) to remove surface particulates generated during processing. Black Si wafers used in this study were supplied by Lam Technology.

### 2.2. EBL-Si Etching Process

The etching process took place in the School of Physics University Cleanroom by Pisu Jiang and Andrew Murray. EBL-Si substrates were fabricated using a multi-step top-down etching approach. A positive-tone e-beam poly(methyl methacrylate) (PMMA) 950 A4 resist was spin coated on top of the initial Si substrates and then subsequently baked at 180  $^{\circ}\text{C}$  for 60 seconds. EBL was then implemented using a Raith Voyager EBL System with a 50 kV electron beam, defining precise nanoscale patterns in the resist.

Following EBL, the patterned substrates underwent chemical development with methyl isobutyl ketone : isopropanol (MIBK:IPA) (1:3 ratio) for 60 seconds and IPA for 30 seconds, followed by an ultrapure water rinse to remove exposed PMMA and reveal the desired pattern while leaving behind the unexposed resist. A 60 nm layer of Ni metal was deposited onto the PMMA resist and exposed Si substrate using thermal evaporation at a pressure of  $5 \times 10^{-6}$  mbar. Following deposition, a selective lift-off process was performed using acetone to dissolve the PMMA resist and remove the Ni on top of it, leaving only the patterned Ni directly on the Si surface behind. The final etching step was carried out using  $\text{SF}_6$  and  $\text{CHF}_3$  gas RIE on the Si substrates themselves for 2 minutes and 2 seconds, employing an Oxford Instruments PlasmaPro 100 Cobra ICP-RIE Etch System with a  $\sim 20$ -30 W radio frequency (RF) bias power. Following the RIE process, the substrate was subjected to a 5-minute  $\text{H}_2\text{SO}_4$  surface cleaning

step to remove the residual Ni mask, leaving the final EBL-defined Si structure. The process can be seen in **Figure 2.1**.

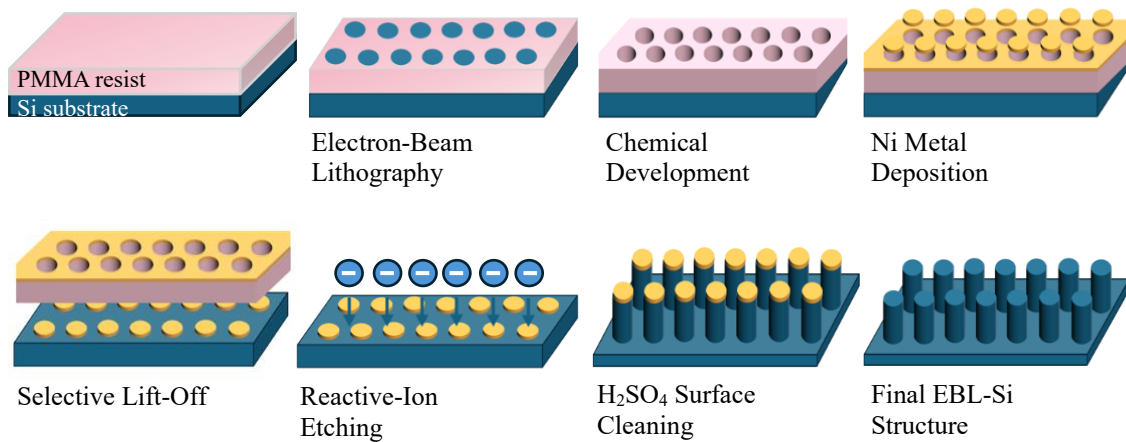


**Figure 2.1:** Schematic representation of the etching process used in the School of Physics University Cleanroom.

For the design of the pattern, three distinct parameters were chosen, dictated by the thickness of the Si pillars ( $T$ ) and the pitch ( $P$ ) - the distance from the centre of one pillar to the centre of the next one: (1)  $T = 200$  nm,  $P = 600$  nm, (2)  $T = 200$  nm,  $P = 800$  nm, and (3)  $T = 200$  nm,  $P = 1000$  nm. This created three EBL-Si designs: (1), T200 P600, (2) T200 P800, (3) T200, P1000. Visualisation of the parameters can be seen in **Figure 2.2**. Each design was selected according to previous work in the University of Bristol Diamond Lab which found that pillars with  $T < 200$  nm were too thin and prone to collapse, while those with  $P < 500$  nm were too closely spaced leading to the subsequent diamond growth completely filling in the gaps between the pillars. Observations were confirmed using SEM, with images provided in **Appendix 5.1**.

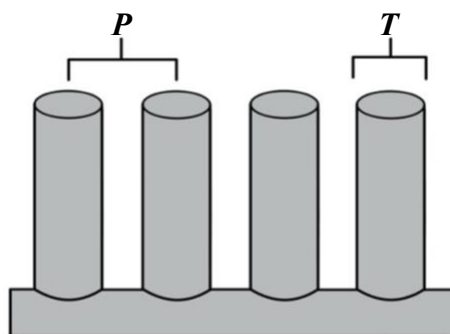


**Figure 2.2:** The parameters used for each EBL design: pitch ( $P$ ) and thickness ( $T$ )

## 2.3. HFCVD

Prior to the seeding process, 10 drops of detonation nanodiamond (DND) in 45 ml methanol was subjected to ultrasonication for 3 hours to deaggregate the particles and achieve a uniform nanoparticle dispersion. The etched EBL-BDD samples were then seeded using this suspension. The process was repeated 3 times to ensure that nanoparticles uniformly covered the entire surface of the sample. The seeded samples were then placed into a HFCVD reactor and heavily-boron-doped diamond was deposited under standard CVD conditions: 20 Torr pressure, Ta filament heated to 2400 K, the substrate has a temperature of approximately 1150 K, and applied current of 25 A (through 3 filaments) with a 1% CH<sub>4</sub>/H<sub>2</sub> gas mixture (200 sccm H<sub>2</sub>, 1 sccm CH<sub>4</sub>) + 0.67 sccm 5% B<sub>2</sub>H<sub>6</sub> 95% H<sub>2</sub> mixture, with the atomic ratio B/C in the gas phase 33,500 ppm. Prior to BDD deposition, the chamber was cleaned with acetone followed by IPA. 3 Ta filaments were placed 3 mm above the surface of the samples. Following various trial and error tests, it was found that uniform and sufficient coating of NCD occurred after 55 minutes of growth. Following growth, the B<sub>2</sub>H<sub>6</sub> and CH<sub>4</sub> gases were switched off, and only H<sub>2</sub> gas was kept in the chamber for a further 2 minutes to give an H-terminated diamond surface.

EBL D-05 (P600) was previously fabricated by Kisty Mao in the Diamond Lab in June 2024, with BDD growth conducted for 30 minutes in the HFCVD reactor until a sufficient coating of NCD was achieved.

A second set of electrodes (f-BDD-01, f-BDD-02, f-BDD-03) were prepared as the control for electrochemical tests. Flat Si wafers were seeded by mechanical abrasion with nanodiamond dust and BDD was grown for 6 h under the same conditions as above to give three f-BDD electrodes with microcrystalline surfaces. While these electrodes are referred to as ‘flat’ diamond in this work, the surface is not perfectly smooth and exhibits a natural roughness arising from the morphology of the different diamond crystallites.

## 2.4. Film Characterisation

Following deposition, analysis was performed on all BDD samples using a JEOL JSM-IT300 scanning electron microscope operating at an accelerating voltage of 15 kV. Laser Raman spectra were recorded at room temperature with a Renishaw 2000 laser Raman spectrometer using green laser excitation (514 nm). Measurements were calibrated using a reference single-crystal diamond and a centre of  $1332\text{ cm}^{-1}$  was chosen.

## 2.5. Electrochemical Analysis

### 2.5.1. Chemicals

Chemical reagents used in electrochemical testing were all of analytical grade. The chemicals used were: potassium nitrate  $\text{KNO}_3$  ( $\geq 99\%$ , Honeywell); sulfuric acid  $\text{H}_2\text{SO}_4$  (95%, Thermo-Fischer Scientific); and furfural FF (99%, Sigma-Aldrich). Standard 0.1 M and 0.5 M stock solutions of  $\text{KNO}_3$  and  $\text{H}_2\text{SO}_4$ , respectively, were prepared. All solutions were prepared using ultrapure water obtained with a Millipore Milli-Q system ( $18.2\text{ M}\Omega\text{ cm}$  at  $25\text{ }^\circ\text{C}$ ).

### 2.5.2. Electrodes

Both EBL-BDD and f-BDD electrodes were prepared for electrochemical analysis as the working electrode using a copper back-plate inside the electrode holder seen in **Figure 2.3**. The holder had a  $4\text{ mm}^2$  radius hole (geometric area of the electrode) to allow for direct contact between the electrolyte and electrode. This design prevented conduction through the Si substrate. Gallium-indium eutectic was used to provide the electrical interface between the back-plate and the electrode. To avoid leaking through the connection between the arm of the holder and the holder itself, polytetrafluoroethylene (PTFE) tape was applied. The reference electrode used was Ag/AgCl submerged in a 3.0 M KCl solution. The counter electrode used was glassy carbon.

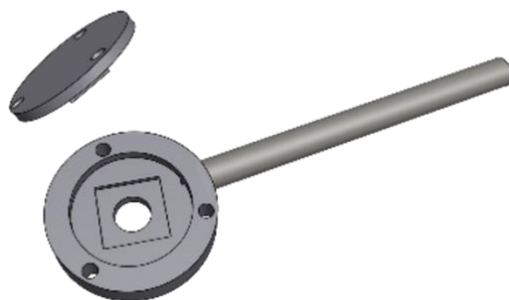


**Figure 2.3:** Image of the electrode holder used for f-BDD and EBL-BDD samples. The electrode holder was provided by Alex Black.

### 2.5.3. Apparatus

Both EBL and f-BDD electrodes were analysed electrochemically *via* cyclic voltammetry (CV) using a potassium nitrate aqueous solution (0.1 M) with a  $\mu$ Autolab Type III potentiostat at room temperature. NOVA 2.1.6 software was used for data collection and analysis. Electrochemical tests were conducted in a glass three-electrode cell containing the electrolyte solution (100 mL), the BDD working, reference, and counter electrode, (**Fig. 2.4**). All CV tests of electrochemical performance, prior to application testing, were performed between the potential range -0.1 to 0.1 V, at a scan rate of  $100 \text{ mV s}^{-1}$ .

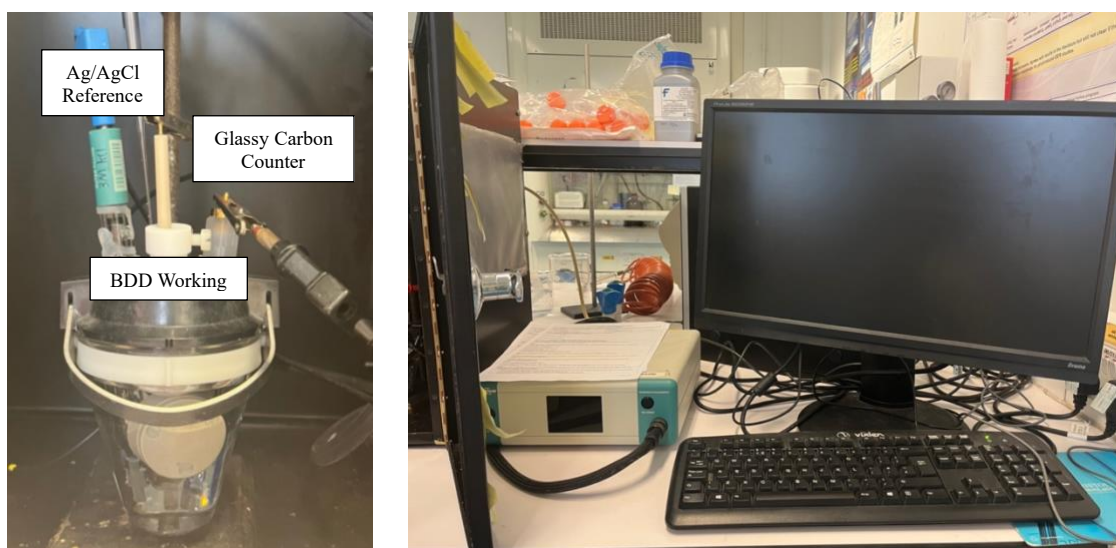


**Figure 2.4:** (a) The electrochemical cell. Left: Ag/AgCl reference electrode; centre: BDD working electrode in electrode holder designed by Alex Black; right: glassy carbon counter electrode. (b)  $\mu$ Autolab Type III potentiostat and computer set up.

Following CV testing, only the highest performing EBL-BDD electrode of each design was selected for further calculations and comparison to the control, f-BDD. This selection was based on  $C_{dl}$  values leading to the final choice of EBL-BDD electrodes: EBL D-05 (T200 P600), EBL D-22 (T200 P800), and EBL D-15 (T200 P1000).

### 2.5.3. Oxygen Termination Treatment

Samples were oxygen-terminated for electrochemical analysis by three different methods, two gas phase and one liquid phase: (i) ozone treatment using a *Jetlight* UVO cleaner for 25 minutes, (ii) 95% sulfuric acid ( $H_2SO_4$ ) + 6.3 g potassium nitrate ( $KNO_3$ ) treatment boiled at 493 K for 2 hours, and (iii) oxygen ( $O_2$ ) plasma treatment for 20 seconds using a converted SEM *Edwards* S150A Sputter-Coater.

### 2.5.4. Furfural Oxidation

Since this was just a preliminary trial of an application, the most stable EBL-BDD electrode (EBL-22 T200 P800) was chosen for oxidation of FF. For these tests the electrode was connected to conductive wire using conductive silver paint covered by epoxy resin. The entire electrode was then covered by Teflon tape with a 7 mm<sup>2</sup> hole (geometrical surface area of the electrode). The electrode was first evaluated for activity for FF oxidation using the set up in **Section 2.6.3**. Electrochemical tests were conducted using 0.5 M  $H_2SO_4$  as the blank electrolyte. To the 100 mL 0.5 M solution of  $H_2SO_4$ , 25 mM of FF was then added. CVs were performed between potentials -1.2 and +2.5 V at a potential scan rate of 100 mV s<sup>-1</sup> to test for the electrode activity for furfural oxidation.

## 3. Results and Discussion

### 3.1. Material Characterisation

#### 3.1.1. Determining the HFCVD Growth Time (SEM)

Visualisation of the electrode surface was achieved by SEM for both material characterisation and to investigate the effect of HFCVD growth time on the morphology of the electrodes. Initially, a 30-minute growth time was decided according to previous work by the Bristol Diamond Lab. Laser Raman spectra indicated that a 30-minute growth time on similarly nanostructured BDD was the optimal for sufficient NCD growth as evidenced by the diminishing intensity of the second-order Si peak. Longer deposition times (45 and 60 minutes) resulted in highly diminished second-order Si peaks suggesting BDD films had potentially grown excessively thick. This overgrowth could increase mechanical stress and therefore reduce conductivity. Due to its supplementary nature these spectra have been provided elsewhere (App. 5.2).

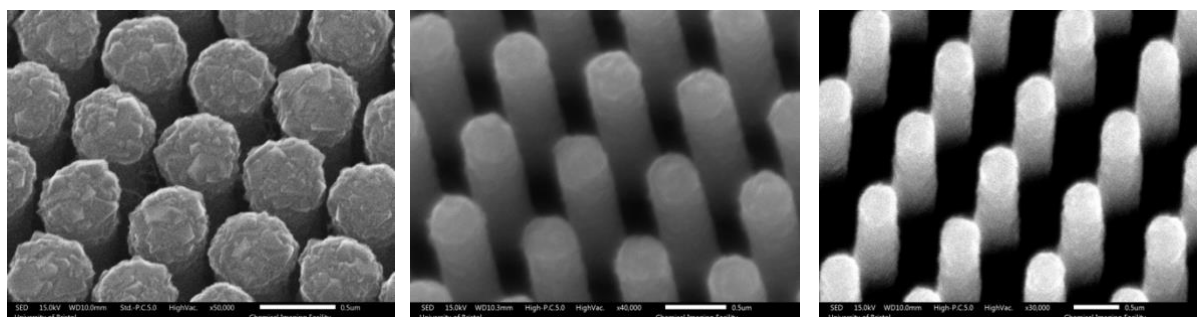


**Figure 3.1:** SEM images of (a) EBL D-05, (b) EBL D-22, (c) EBL D-15 after 30 minutes of growth time in the HFCVD reactor.

**Figure 3.1** shows SEM images of the EBL-BDD surfaces after this initial 30-minute coating. **Table 3.1** reflects the diamond film thickness and gap between each of the BDD-coated Si pillars. For EBL BDD electrodes EBL D-22 and EBL D-15, the diamond film thickness reached a maximum of 140 nm. Based on established literature indicating that increased BDD film thickness enhances electrochemical performance, a baseline minimum diamond film thickness of 150 nm was decided necessary before electrodes were tested for electrochemical performance.<sup>126</sup> As a result, further coating was carried out to achieve the desired film thickness

and optimise the electrochemical properties of the electrodes. For the EBL-BDD electrode EBL D-05, 30 minutes provided a sufficient diamond film thickness of  $>150$  nm and this electrode was deemed suitable for electrochemical testing. This is presumed to be due to the phenomenon whereby B diffuses into the walls of the HFCVD reactor and later diffuses back into the gas mixture during deposition due to the increase in temperature and pressure, causing increased, unexpected doping.<sup>127</sup> As mentioned in **Section 2.3**, EBL D-05 was grown prior to the deep cleaning of the inside of the HFCVD reactor in June 2024. Consequently, a shorter growth time was reasonable as residual B from previous depositions may have led to a higher concentration of B in the gas phase, thereby accelerating the growth of CVD BDD. Although the diamond film thickness of the EBL D-05 electrode was adequate, exceeding the target minimum at 173 nm, the narrow inter-pillar spacing of just 62 nm raised concern regarding electrolyte accessibility. The confined geometry could restrict the full utilisation of the available electrode surface area, giving an underestimation for  $C_{dl}$  in future testing. Consequently, although increasing the density of nanostructures theoretically enhances surface area and capacitance, precise control over diamond film thickness is crucial in narrow pitch EBL structures. Excessive growth can lead to the connection of adjacent pillars, which not only reduces the effective surface area but also eliminates the purpose of the nanostructure design.

**Table 3.1:** Diamond film thickness and the gap between the nanostructured pillars after 30 minutes diamond growth.

Electrode	Diamond Film Thickness / nm	Gap Between Pillars / nm
EBL D-05	173	62
EBL D-22	140	341
EBL D-15	122	556

**Figure 3.2** presents the EBL-BDD designs, EBL D-22 and EBL D-15, after a growth time of 55 minutes. The corresponding film thickness and inter-pillar spacing for these structures are summarised in **Table 3.2**. A minimum diamond film thickness of 171 nm revealed the development of sufficient BDD film thickness as deposition time increased. A growth time of 55 minutes in an HFCVD reactor aligns with previous findings by Simon et. al that significant growth of NCD is found after 50 minutes.<sup>128</sup>

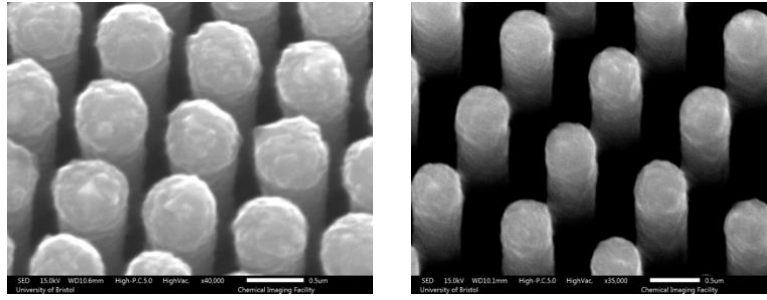


**Figure 3.2:** SEM images of (a) EBL D-22 and (b) EBL D-15 after 55 minutes of growth time in the HFCVD reactor.

The reduction of inter-pillars gaps for both the EBL D-22 and EBL D-15 electrodes suggested increased lateral growth of the BDD film along sidewalls while still maintaining substantial distance to prevent coalescence between pillars to maintain open pathways for electrolyte flow.

**Table 3.2:** Diamond film thickness and the gap between the nanostructured pillars after 55 minutes diamond growth.

Electrode	Diamond Film Thickness / nm	Gap Between Pillars / nm
EBL D-22	253	122
EBL D-15	171	466

The significant difference in BDD growth between 30 and 55 minutes could be accredited to the process mentioned above whereby B diffuses out of the walls of the reactor into the gas mixture. Furthermore, growth rate in an HFCVD reactor has been observed to not be strictly linear, due to an initial nucleation period during which BDD growth does not immediately occur. Instead, this phase is characterised by the formation of diamond nucleation sites on the substrate which act as the foundation for subsequent crystal growth. Once sufficient nucleation has occurred the diamond film then begins to form, and the growth rate increases before stabilising.<sup>129</sup>

SEM images confirmed the growth of nanocrystalline BDD on the surface of the EBL-Si substrates and that films were continuous over the entire surface of the Si pillars. However, measurements for both diamond film thickness and inter-pillar spacing estimated based on SEM imaging are subject to limitations in resolution and contrast, introducing potential uncertainties in subsequent surface area calculations.

### 3.1.2. Investigating Boron Concentration (Laser Raman)

Visible laser Raman spectra taken of the EBL-BDD electrodes seen in **Figure 3.3** suggested all samples exhibited the characteristic peaks of BDD thin diamond films. The peak at  $\sim 1300\text{ cm}^{-1}$  reflected the first-order phonon mode of  $\text{sp}^3$  diamond carbon. This peak shifted from the characteristic  $1332\text{ cm}^{-1}$  due to boron incorporation and nanostructuring effects. The B peak at  $1220\text{ cm}^{-1}$  is a key signature of synthesised BDD associated with a disorder-induced mode caused by boron in the diamond lattice. A second-order Si peak can be seen at  $950\text{ cm}^{-1}$  caused by the EBL-Si substrate beneath the EBL-BDD. For both EBL D-05 and EBL D-15 the diamond peak is slightly more intense than the Si peak suggesting that the EBL-Si substrate was adequately coated in BDD. Since the BDD films were relatively thin, measuring only 170-255 nm, this likely explains the prominence of the Si peak. For EBL D-22, the Si peak appeared more intense than the diamond peak which may be attributed to the limited thickness of the BDD films or incomplete coverage of the EBL-Si, particularly at the base of the Si pillars. Furthermore, both D and G graphitic ( $\text{sp}^2$  containing diamond- $\pi$  bonds) peaks were visible in all spectra at  $\sim 1355\text{ cm}^{-1}$  and  $1575\text{ cm}^{-1}$ , respectively. In BDD with a high level of doping, the broadening of peaks at  $1220\text{ cm}^{-1}$  indicated a B/C ratio exceeding 400 ppm. Additionally, a broad peak at  $\sim 500\text{ cm}^{-1}$  started to obscure the expected sharp 1<sup>st</sup>-order Si peak when the B/C ratio exceeds 1000 ppm.<sup>130</sup> All EBL samples demonstrated a first-order Si peak at  $\sim 520\text{ cm}^{-1}$  (**App. 5.3**) suggesting a B/C ratio  $< 1000$  ppm. However, any spectra inclusive of this peak were negligible since all other informative peaks were dwarfed by the strong first-order Si peak. Despite this, all samples demonstrated the broad features at  $1220\text{ cm}^{-1}$  suggesting a B/C ratio  $> 400$  ppm. This observation is likely due to the discrepancy between the high nominal B/C ratio of 33,000 ppm in the feed gas of the HFCVD reactor and the actual incorporation efficiency of B into the diamond lattice. Given that most of the B species are removed via the pump system, the effective B concentration in the deposited film is reduced to approximately 1%, which accounts for the observed Raman response.

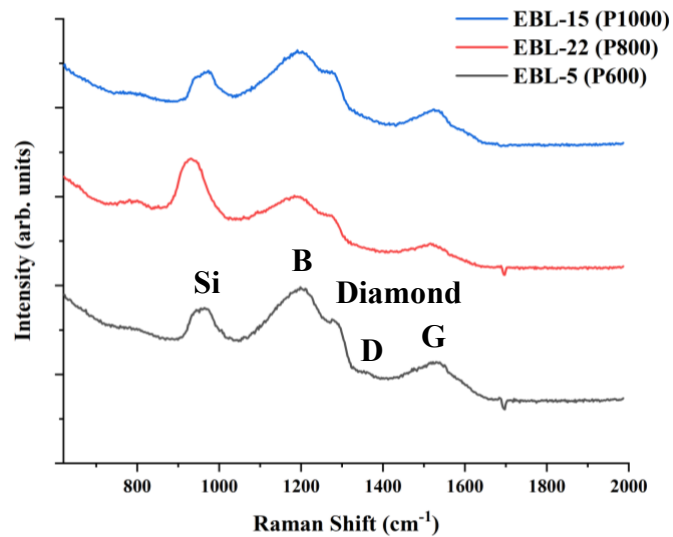


**Figure 3.3:** Laser Raman spectra of EBL D-05 (P600), EBL D-22 (P800), and EBL D-15 (P1000) BDD electrodes using 514 nm laser excitation. Each spectrum has been offset vertically for comparison

Broadening features occurred due to Fano interference leading to asymmetrical shapes.<sup>131</sup> The scattering of phonons as a result of grain boundaries in NCD shortens the lifetimes of the phonons leading to broader Raman lines.<sup>132</sup> The peaks in NCD are wider compared to MCD due to the higher grain boundary density per volume. Consequently, the spectra provided evidence supporting the successful synthesis of heavily B-doped NCD films.

## 3.2. Electrochemical Performance

The reliability of all measured  $C_{dl}$  values was influenced by instrumental precision, particularly with respect to the potentiostat resolution and baseline drift. Care was taken to minimise this effect by ensuring stable temperature conditions, degassing the electrolyte with Ar prior to measurements, and maintaining a clean electrode surface between scans.

### 3.2.1. Effect of Oxygen Termination Pre-Treatments

As mentioned in **Section 1.6.4**, surface modification of electrodes post-CVD is crucial for optimal performance in aqueous electrolyte solutions. Therefore, to enhance the contact between the EBL-BDD and f-BDD electrodes and the electrolyte solution, samples were pre-treated by oxygen termination which altered the charge-transfer kinetics and increased wettability by ensuring a hydrophilic electrode surface. A CV was recorded before and after each oxygen termination treatment of EBL-BDD electrodes of design P600 to assess the efficiency of each treatment method. There were notable increases in  $C_{dl}$  following all oxygen-termination treatments. The resulting CVs revealed a significant difference between the  $H_2SO_4$  (AOT) and  $O_2$  plasma (AOP) treatment in comparison to the ozone (AOZ) treatment, (**Fig 3.4**).

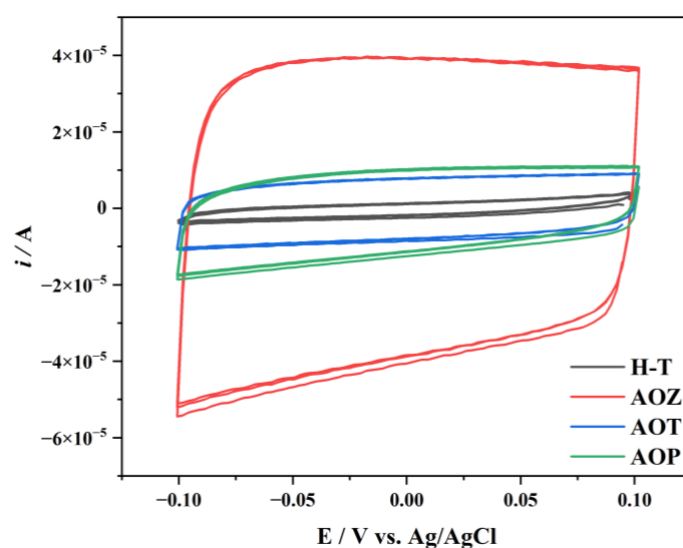


**Figure 3.4:** CV of EBL BDD samples of the T200 P600 design after different oxygen treatments:  $O_3$  (AOZ);  $H_2SO_4$  (AOT); and  $O_2$  plasma (AOP) in comparison to a H-terminated electrode of the same design (H-T).

The  $C_{dl}$  values recorded for each oxygen treatment can be seen in **Table 3.3**. Among the methods evaluated, AOZ treatment demonstrated significantly greater effectiveness, achieving a  $C_{dl}$  value of  $794.2 \mu\text{F cm}^{-2}$  relative to the  $C_{dl}$  value of the H-terminated reference electrode of  $30.8 \mu\text{F cm}^{-2}$ . This improvement notably exceeded the improvements observed for both the AOP and AOT treatments. AOZ was considered most effective due to problems with the other two treatments. Concentrated  $\text{H}_2\text{SO}_4$  is a strong oxidiser and may be too aggressive for thin BDD films such as those fabricated for this report. Other strong acids have been seen to alter the crystal morphology of BDD following anodic polarisation leading to a decrease in electrochemical activity.<sup>133</sup> Undoped diamond has been shown to undergo etch during AOP even at short exposure times of 60 seconds. Similarly, at a longer duration of 20 minutes, AOP has been reported to etch the surface of CVD diamond, despite the etching resistance provided by the incorporation of B within the film.<sup>134</sup> This suggests that even at shorter durations, reactive oxygen radicals may still attack the carbon-carbon bonds in the diamond lattice, forming volatile compounds that desorb from the diamond surface, resulting in a thinner BDD film. AOZ is much gentler by comparison to these other two methods, oxidising the surface more uniformly without significant etching. However, these are suggestions based on the nature of each process and are not proven reasons as to why AOZ is most effective at improving the  $C_{dl}$  of EBL-BDD samples.

**Table 3.3:** Double-layer capacitance values for each oxygen termination treatment.

Oxygen Treatment	$C_{dl} / (\mu\text{F cm}^{-2})$
H-T	30.8
AOZ	794.2
AOT	155.3
AOP	213.8

### 3.2.2. EBL-BDD Double Layer Capacitance Performance

CVs to evaluate electrochemical performance of EBL-BDD samples were recorded in the presence of background aqueous electrolyte solution ( $0.1 \text{ M KNO}_3$ ) to gain the double-layer capacitive current. **Figure 3.5** shows the CVs at scan rate  $100 \text{ mV s}^{-1}$  over the potential range of  $-0.1 \text{ V}$  to  $0.1 \text{ V}$  (vs Ag/AgCl) for the most successful EBL-BDD sample of each design. All

EBL-BDD samples demonstrated the expected shape of a quasi-rectangle for interfacial double-layer charging.<sup>135</sup> This is also indicative of a good electrode material for electrochemical double-layer capacitors. However, both EBL D-22 (P800) and EBL D-15 (P1000) exhibited a slight slant in the current-voltage curves. This slanted behaviour, noticeable in both the forward and reverse sweeps, is characteristic of minor leakage currents, which deviate from the ideal behaviour. This is typically due to side reactions at the electrode surface. Trace impurities in the  $\text{KNO}_3$  electrolyte or adsorption of small amounts of contaminants could cause these small leakage currents. Although these defects manifested as a slant in the CVs, their impact on the  $C_{dl}$  of both electrodes is minimal. It does not interfere significantly with the peak current and although it may slightly distort the shape of the voltammogram, it does not compromise the representation of electrochemical performance extensively farther than slight discrepancies in the measured current which may have led to overestimations for the  $C_{dl}$  values.

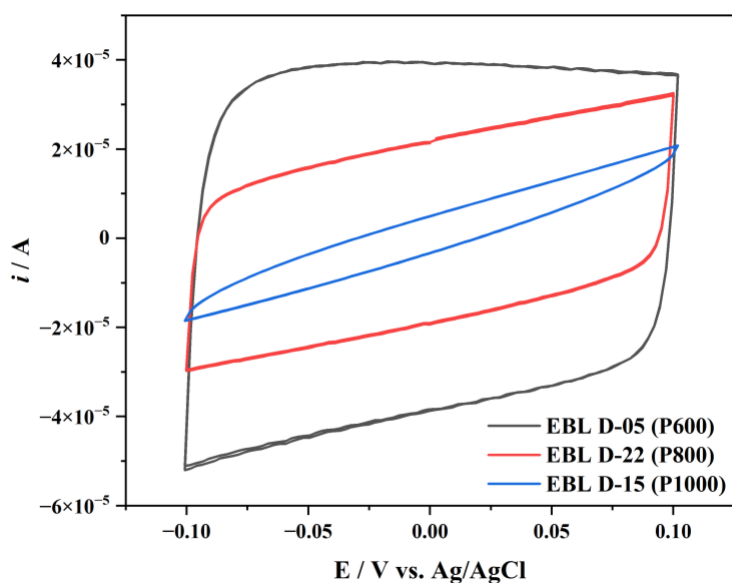


**Figure 3.5:** CV of each EBL BDD electrode in background electrolyte 0.1 M  $\text{KNO}_3$ ,  $\nu = 100 \text{ mV s}^{-1}$

The measured  $C_{dl}$  values for the EBL-BDD electrodes are summarised in **Table 3.4**. The EBL D-05 electrode exhibited the highest capacitance, reaching  $794.2 \mu\text{F cm}^{-2}$ . This represented a significant enhancement in comparison to other designs EBL D-22 and EBL D-15 with  $404.3 \mu\text{F cm}^{-2}$  and  $87.3 \mu\text{F cm}^{-2}$ . As mentioned in **Section 1.5.4**, the  $C_{dl}$  is proportional to the surface area of each electrode influenced by the pitch ( $P$ ) of the electrode design. The trend in

capacitance strongly correlated with the pattern pitch of the nanostructures, where a reduced pitch (P600) yielded a higher density of nanopillars, and thus a larger electrochemically active surface area. The increase in surface area enhances charge accumulation at the electrode-electrolyte interface in double-layer charging, directly contributing to the observed rise in  $C_{dl}$  value. These results clearly demonstrated that finer nanostructuring achieved through closer pitch designs significantly improved the electrochemical performance of BDD electrodes constructed by EBL.

**Table 3.4:** Double-layer capacitance ( $C_{dl}$ ) values for each EBL BDD electrode in  $\mu\text{F cm}^{-2}$

Electrode	$C_{dl} / (\mu\text{F cm}^{-2})$
EBL D-05 P600	794.2
EBL D-22 P800	404.3
EBL D-15 P1000	87.3

In comparison to literature of similar BDD electrodes with structures on the nanoscale, the work of Lu et al., who developed three-dimensional porous BDD films via HFCVD, achieved a  $C_{dl}$  value of  $17.54 \text{ mF cm}^{-2}$ . This provides an interesting benchmark for evaluating the performance of the EBL-BDD electrodes developed in this study. The much larger capacitance was attributed to the creation of densely interconnected porous networks that created an inherently higher effective surface area. However, it is important to consider that the fabrication method used to create this large surface area involves a template-free approach which does not offer the same degree of structural precision as EBL which could influence consistency across electrodes. This comparison emphasises a key trade-off between maximising surface area through high porosity and achieving precise structural control for future electrode optimisation. Comparable or lower capacitance values have been reported in other studies employing micro- and nanocrystalline diamond following the same approach to this study of improving surface area. Suman et al. found a  $C_{dl}$  value of  $85.2 \mu\text{F cm}^{-2}$  for ultra-nanocrystalline diamond vertically aligned BDD nanopillars in  $1 \text{ M Na}_2\text{SO}_4$  solution fabricated by Au mask-assisted RIE, similar to that of the EBL D-15 electrode.<sup>136</sup> The difference in specific capacitance to better performing electrodes in this work can be attributed to the different electrolyte solution which may offer different ion mobility and double-layer formation characteristics since  $\text{Na}_2\text{SO}_4$  is more

commonly used for assessing supercapacitor capabilities. However, the substantial disparity in capacitance values suggest that structural factors are the dominate factor for the observed performance enhancement since all other factors are almost identical. These findings reinforce the value of EBL as a fabrication strategy for the development of high-performance electrochemical devices based on BDD. Additionally, Sartori et al. reported a  $C_{dl}$  value of 660  $\mu\text{F cm}^{-2}$  using laser-induced periodic surface structuring (LIPSS), aligning closely with the performance of the best-performing EBL-BDD electrode in this study. This similarity not only reinforces the validity of the capacitance values achieved here but underscores the effectiveness of both techniques in enhancing electrochemical performance through nanoscale surface texturing. Of particular interest, the slightly higher capacitance value of the EBL D-05 of this study suggests that, despite the efficiency of laser texturing, the deterministic nanostructuring of EBL provides a marginally more effective result.

Based on the laser Raman results in **Section 3.1.2**, the discrepancies in capacitance between EBL D-05 and EBL D-22 may be attributed to the possible inconsistent coverage of BDD on the EBL D-22 electrode, which could have resulted in a significantly lower capacitance value. Both EBL D-22 and EBL D-15 are designed to have larger gaps between the pillars for future work involving metal deposition, and therefore the smaller capacitance is expected, due to the difference in surface area. However, these electrodes are designed for a different purpose than EBL D-05, and the difference in capacitance does not diminish their capability as efficient electrodes.

### 3.2.3. Control f-BDD

Control electrodes f-BDD-01, f-BDD-02, and f-BDD-03 were tested for electrochemical performance under the identical conditions to those used for the EBL-BDD electrodes, allowing for direct comparison. CV was performed in 0.1 M  $\text{KNO}_3$  electrolyte at a scan rate of 100  $\text{mV s}^{-1}$  over a potential window of -0.1 V to 0.1 V (vs. Ag/AgCl). **Figure 3.6** illustrates overlaid CVs of all three f-BDD electrodes where similar shapes were observed overall. However, minor deviations were noted, with signs of leaking resistance for both f-BDD-01 and f-BDD-02, as indicated by slight slanting of the voltammogram baseline. Despite this, all control electrodes produced voltammograms characteristic of capacitive behaviour for comparison with the EBL-BDD electrodes.

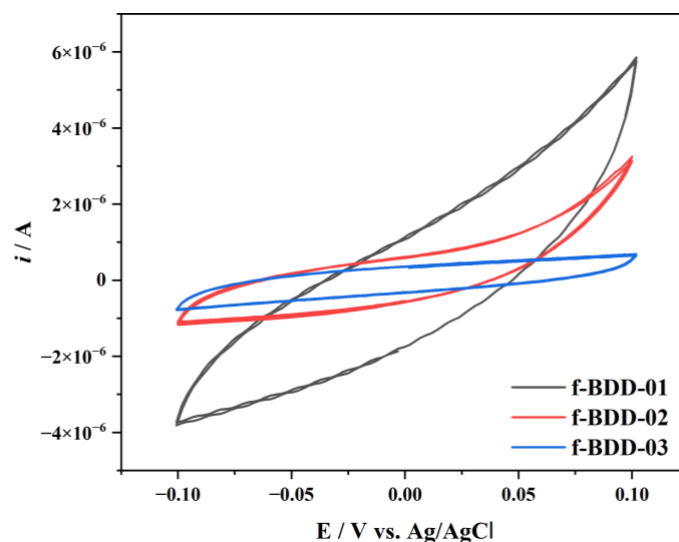


**Figure 3.6:** CV of each f-BDD electrode in background electrolyte 0.1 M KNO<sub>3</sub>,  $\nu = 100 \text{ mV s}^{-1}$ .

The  $C_{dl}$  values ranged from 28.9 to 7.0  $\mu\text{F cm}^{-2}$  for the control microcrystalline samples f-BDD-01, f-BDD-02, and f-BDD-03 in the presence of KNO<sub>3</sub> as seen in **Table 3.5**. The reproducibility of the electrochemical measurements for the reference electrode was confirmed across three independent samples, though minor deviations were observed, likely due to slight variations in diamond film thickness and oxygen termination processes. To establish a reliable reference for comparison with the EBL-BDD samples, an average  $C_{dl}$  value was determined from each sample of 15.7  $\mu\text{F cm}^{-2}$ . As previously mentioned in **Section 1.5.4**, literature values for f-BDD typically range from approximately 3-10  $\mu\text{F cm}^{-2}$ .<sup>35,90,137</sup> However, as reported by Baluchová et al., alternating B/C can significantly influence the geometric  $C_{dl}$  values for f-BDD.<sup>138</sup> Accordingly, the high B/C ratio used in this study is expected to contribute to the elevated average  $C_{dl}$  value observed.

**Table 3.5:** Double-layer capacitance ( $C_{dl}$ ) values for each f-BDD sample giving an average value of 15.7  $\mu\text{F cm}^{-2}$

Electrode	$C_{dl} / (\mu\text{F cm}^{-2})$
f-BDD-01	28.9
f-BDD-02	11.3
f-BDD-03	7.0

### 3.2.4. f-BDD vs. EBL-BDD

For clarity, only the best-performing EBL-BDD electrode, EBL D-05, was considered for comparison to f-BDD (**Fig. 3.7**). f-BDD-01 was chosen for visual representation purposes, however calculations for comparison utilised the average  $C_{dl}$  value of  $15.7 \mu\text{F cm}^{-2}$ . There is a significant difference between the average  $C_{dl}$  of the f-BDD samples and the nanostructured EBL-BDD sample. This is expected since double-layer charging, and therefore  $C_{dl}$ , increases with larger surface areas, particularly in nanostructured electrodes.<sup>139</sup>

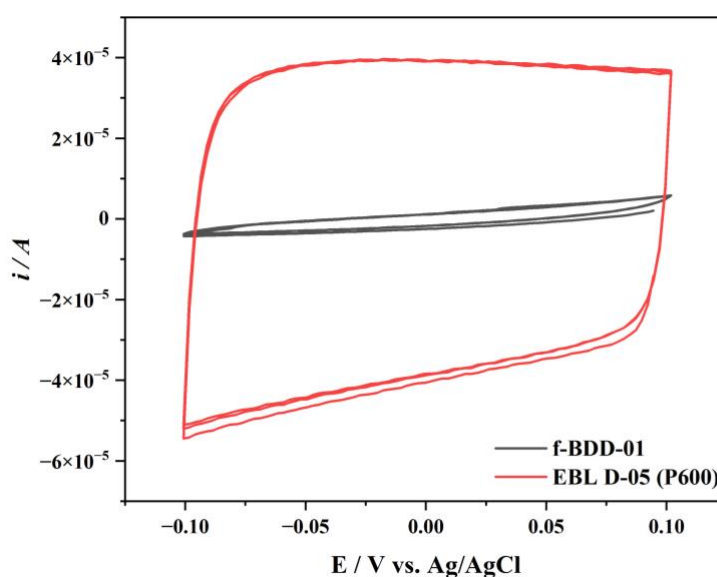


**Figure 3.7:** CV of f-BDD-01 in comparison to EBL D-05 in background electrolyte 0.1 M  $\text{KNO}_3$ ,  $\nu = 100 \text{ mV s}^{-1}$

Values seen in **Table 3.6** show substantially higher  $C_{dl}$  values across all EBL-BDD samples and indicate that the  $C_{dl}$  of the most capacitive electrode (EBL D-05) is approximately 50.6 times greater than that of f-BDD. This can be directly attributed to the enhanced effective surface area of the EBL-BDD electrodes as a result of their nanostructured design. Similarly, the EBL D-22 electrode recorded a  $C_{dl}$  value with a 25.8-fold increase over the f-BDD reference. While lower than EBL D-05, this performance still reflects effective utilisation of increased surface roughness and structured BDD in comparison to unstructured f-BDD. The EBL D-15 electrode, though displaying the lowest capacitive difference of the three structured designs, still achieved a 5.6-fold enhancement relative to the flat electrode. This result suggests that while increased spacing between the pillars reduced total surface area, it nonetheless

provided a substantial improvement over the unstructured counterpart, validating the effectiveness of even modest nanostructuring in enhancing electrode performance. The differences in  $C_{dl}$  highlights the crucial role of structural modifications to the electrode surface in electrochemical performance amongst BDD electrodes specifically.

**Table 3.6:** Double-layer capacitance ( $C_{dl}$ ) values for flat and nanostructured BDD electrodes, and their relative enhancement compared to flat BDD.

Electrode	$C_{dl} / (\mu\text{F cm}^{-2})$	$C_{dl} \times \text{f-BDD}$
f-BDD	15.7	-
EBL D-05 P600	794.2	50.6
EBL D-22 P800	404.3	25.8
EBL D-15 P1000	87.3	5.6

The magnitude of the higher  $C_{dl}$  values for nanostructured or porous BDD electrodes in comparison to that for f-BDD is consistent with published findings where increased roughness and effective surface area improve electrochemical activity. Notably, research by May et. al demonstrated an exceedingly larger  $C_{dl}$  value for BDD-coated bSi of a magnitude of up to 220 times in comparison to a commercial f-BDD electrode with a  $C_{dl}$  value of  $2.9 \mu\text{F cm}^{-2}$ .<sup>35</sup> Aside from the significantly lower  $C_{dl}$  value used for the reference f-BDD electrode, which contributes to the disparity between the results found in this study and the study conducted by May et al., it is important to note that bD films vary significantly in structure and composition. These differences make accurate surface area quantification more challenging. Furthermore, it is difficult to ensure reproducibility across different bD electrodes due to unpredictable pillar formation. Therefore, while bD electrodes are reported to have promising capacitance enhancements, the EBL-BDD electrodes developed in this study demonstrate comparatively superior capacitive performance relative to bD, reflecting the effectiveness of nanostructuring uniform and reproducible electrodes. This also highlights the promise of EBL-BDD electrodes for electrochemical applications requiring advanced capacitive performance, particularly relative to other previously documented nanostructured electrodes. Knittel et al. reported an approximately. 80-fold increase in  $C_{dl}$  for nanostructured BDD electrodes relative to a flat diamond film.<sup>137</sup> However, the reference flat electrode exhibited a relatively low  $C_{dl}$  value of  $6.5 \mu\text{F cm}^{-2}$  for comparison and, as stated previously, the present study used a higher

experimental average of  $15.7 \mu\text{F cm}^{-2}$  for the flat electrode. Considering the difference, the nanostructured EBL-BDD electrodes in this work provided a more representative evaluation of the impact of nanostructuring, demonstrating a larger capacitive increase relative to comparable f-BDD values reported in the literature.

Further reinforcing these findings, the study by Kondo et al. demonstrated a nanostructured porous BDD electrode fabricated via a two-step thermal treatment process, including microwave plasma-assisted chemical vapour deposition (MPCVD), which achieved a  $C_{dl}$  of  $140 \mu\text{F cm}^{-2}$  – an enhancement of around 40 times relative to as-deposited planar BDD. Kondo et al. employed a Si wafer substrate and a comparable atomic B/C ratio, enabling a direct and meaningful comparison with the findings of this report.<sup>140</sup> The value of  $140 \mu\text{F cm}^{-2}$  closely parallels the values seen in this study for the EBL D-15 and EBL D-22 electrodes and is notably exceeded by the EBL D-05 electrode. The better capacitance value can be attributed to the methodology differences between the methods of this study and those chosen by Kondo et al. Thermally induced porosity inherently suffers from less control over pore size distribution and surface uniformity in comparison to EBL structuring. This advantage likely contributed to the higher capacitance values observed, as uniform nanoscale pillar arrays provide optimised electrolyte accessibility. Therefore, this work demonstrates not only competitive but for the most capacitive electrode design, EBL D-05, superior performance to other nanostructured BDD systems reported in the literature.

### 3.2.5. Determinations of Surface Area

#### **Geometric Surface Area**

On analysis of the electrochemical properties of BDD electrodes, the geometric surface area ( $A_g$ ) is crucial in calculating the  $C_{dl}$  in this report. A geometric surface area of  $0.5 \text{ cm}^2$  ( $\pi \times (0.4 \text{ cm}^2)^2$ ) was calculated from the exposed area of the electrode holder shown in **Figure 2.3** and used for all BDD electrodes, providing a consistent reference for calculations.

#### **Actual Surface Area**

In addition to the geometric surface area used in  $C_{dl}$  calculations, the actual surface area ( $S_{\text{Actual}}$ ) of each EBL BDD electrode must account for the additional surface contributed by the three-dimensional micro-structured features introduced by the EBL-Si template and

subsequent CVD-grown BDD layer thickness.  $S_{\text{Actual}}$  of the EBL BDD electrodes was calculated using **eqn (3.1)**:

$$S_{\text{Actual}} = \left(\frac{10 \times 10^6}{P}\right)^2 \times 2\pi \left(\frac{T}{2} + D\right) \times H + (10 \times 10^6)^2 \quad (3.1)$$

where  $P$  is the pitch of the EBL-Si pillars,  $T$  is the thickness of each EBL-Si pillar,  $D$  is the thickness of the BDD layer, and  $H$  is the height of the EBL-Si pillars. This equation uses the planar surface area of the Si substrate in combination with the surface area contributed by the curved sidewalls of the pillars in each electrode design to obtain a more representative surface area estimation. By accounting for the nanostructured features of the EBL BDD electrodes, the actual surface area becomes significantly greater than the geometric projection used for simplified calculations (**Table 3.7**). These features provide an increased number of active sites for electrochemical reactions for improved electrode performance. The  $S_{\text{Actual}}$  value for the reference f-BDD electrode has been normalised to 1 for comparative purposes.

**Table 3.7:** Actual surface area ( $S_{\text{Actual}}$ ) of each BDD electrode.

Electrode	$S_{\text{Actual}} / (10^{14} \text{ nm}^2)$
f-BDD	1
EBL D-05	10.5
EBL D-22	7.9
EBL D-15	4.4

In contrast to the normalised f-BDD reference, the nanostructured electrodes demonstrated marked increases in actual surface area, with the EBL D-05 design achieving the highest  $S_{\text{Actual}}$  value of  $10.5 \times 10^{14} \text{ nm}^2$  – a tenfold increase over the flat electrode. This can be attributed to the fine pitch and dense pillar arrangement, which maximises surface exposure to the electrolyte solution. The higher surface area naturally provides more active sites for charge accumulation, reflected in the higher  $C_{\text{dl}}$  value for EBL D-05. The gradual reduction in surface area from EBL D-05 to EBL D-15 reflects the initial design choice in pillar spacing, as larger gaps and pillars reduce the total accessible surface area. These findings provide quantitative support for the electrochemical performance quoted earlier in this study, where increased surface area is shown to play a critical role in elevating the double-layer capacitance of BDD

electrodes. The correlation between design parameters and resulting surface area underlines the tunability of EBL methods.

**Figure 3.8** provides a schematic illustration of the difference between  $A_g$  and  $S_{\text{Actual}}$  of the EBL-BDD electrodes when positioned in the electrode holder. The visual distinction in Figure 3.8 highlights the importance of considering the actual surface area following  $C_{\text{dl}}$  calculations since reliance solely on the geometric area would lead to a significant underestimation of the potential of the electrodes.

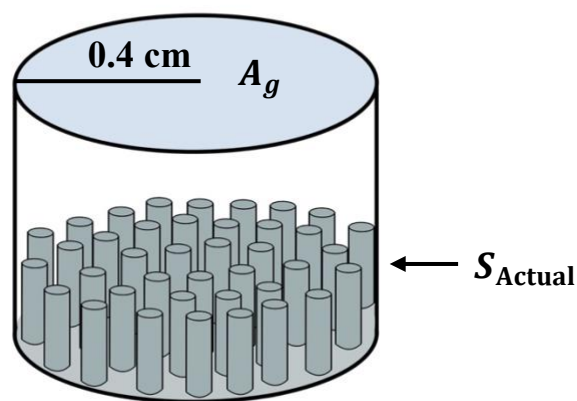


**Figure 3.8:** Visual representation of the geometric surface area ( $A_g$ ) and actual surface area ( $S_{\text{Actual}}$ ) of EBL BDD electrodes when in the electrode holder (not to scale).

### Relative Effective Surface Area

To quantitatively evaluate the impact of nanostructuring on the electrode surface properties, an estimation of the relative effective surface area of each BDD electrode was determined based on the ratio of reference f-BDD to EBL-BDD  $C_{\text{dl}}$  values, as described previously in **Table 7**. The calculation used is shown in **eqn (3.2)**:

$$\text{Relative Effective Surface Area} = \frac{C_{\text{dl,structured}}}{C_{\text{dl,flat}}} \times A_g \quad (3.2)$$

The relative surface area provides a direct comparison of the electrochemically active surface between nanostructured electrodes fabricated via EBL and the f-BDD reference electrode, which has, again, been normalised to a value of 1. This approach allowed for the evaluation of

how variations in nanostructuring parameters influence the available active area for electrochemical processes. The results for each electrode design are summarised in **Table 8**.

**Table 3.8:** Relative effective surface area of each BDD electrode.

Electrode	Relative Effective Surface Area / ( $10^{14} \text{ nm}^2$ )
f-BDD	1
EBL D-05	25.4
EBL D-22	12.9
EBL D-15	2.8

Significant enhancement in relative effective surface area was observed for the EBL BDD electrodes compared to the f-BDD reference. The EBL D-05 electrode exhibited the largest increase, with a relative effective surface area of  $25.4 \times 10^{14} \text{ nm}^2$ , indicating more than a 25-fold improvement over the f-BDD electrode. This substantial enhancement is assumed to be attributed to the higher density and finer features of the nanostructure pattern, which increase both the number of active sites and the overall interfacial area available for electrochemical reactions. In comparison, the EBL D-15 electrode demonstrated a more modest increase, with a relative surface area of  $2.8 \times 10^{14} \text{ nm}^2$ , suggesting that while nanostructuring does enhance surface area, the extent is highly dependent on the specific parameters employed.

The findings of Lee et al. report a threefold increase in effective surface area for BDD nanowire electrodes compared to planar BDD, as determined by CV measurements.<sup>141</sup> This enhancement is closely aligned with the performance of the EBL D-15 electrode developed in this study. This similarity suggests that the level of nanostructuring achieved in EBL D-15 is comparable to the nanowire approach employed by Lee et al. However, the more advanced designs explored in this work, the EBL D-05 and EBL D-22 electrodes, demonstrated substantially greater enhancements than those reported by Lee et al. This comparison highlights the effectiveness of EBL in maximising surface area. The larger relative effective surface area of the EBL D-05 and EBL D-22 electrodes compared to both EBL D-15 and the nanowire electrodes can be attributed to a couple factors. The use of the EBL process enabled precise control over pattern density, allowing for a higher pillar density to increase the total active surface area. Furthermore, in nanowires, close-packed structures can shield sidewalls from electrolyte access. However, the

spacing between pillars is well-defined in EBL designs, which likely facilitated improved electrolyte diffusion.

### 3.3. Furfural Oxidation

#### 3.3.1. Activity of EBL-BDD for Furfural Oxidation

At present, there are no reported studies in the literature concerning the use of EBL-BDD electrodes for the oxidation of FF, providing no direct point for comparison for this novel application. Therefore, any anticipated electrochemical behaviour is largely based upon the performance of diamond and other carbon-based electrodes in acidic media, particularly in relation to the OER. All EBL-BDD designs and the control f-BDD were assessed for activity for FF oxidation in 25 mM FF in 0.5 M H<sub>2</sub>SO<sub>4</sub> aqueous solution at a scan rate of 100 mV s<sup>-1</sup>. The EBL D-22 (P800) electrode exhibited the most stability and the only anodic peak for FF oxidation and therefore was selected for analysis and comparison to literature. CVs were performed to evaluate the electrochemical activity of EBL D-22 for FF oxidation in acid. Generally, FF oxidation in alkaline media is considered more favourable in comparison to acidic media however, since this was a preliminary trial and time was limited, the most readily available chemicals were used for experimentation.

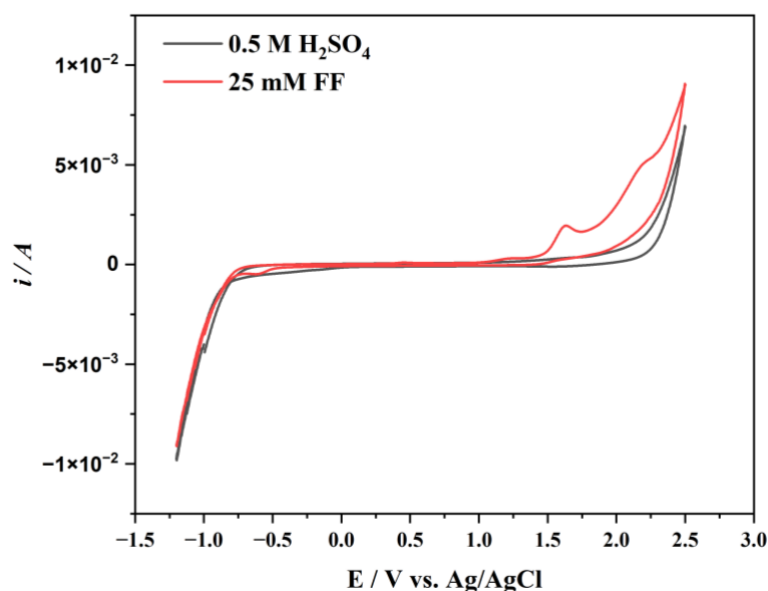


**Figure 3.9:** CV of 0.5 M H<sub>2</sub>SO<sub>4</sub> and 0.5 M H<sub>2</sub>SO<sub>4</sub> + 25 mM FF,  $\nu = 100 \text{ mV s}^{-1}$  with EBL D-22.

**Figure 3.8** presents the CV of the EBL D-22 electrodes, covering both the higher potential region corresponding to the OER and lower potential region corresponding to the HER. The CV response in the presence of FF revealed a distinct anodic peak, the onset of FF oxidation and confirming catalytic activity towards this reaction. The well-defined peak at 1.6 V vs. Ag/AgCl provided clear evidence of the electrochemical conversion of FF. While literature on FF oxidation specifically using BDD electrodes is not currently available, as previously stated, this result for FF oxidation aligned closely with reported oxidation potentials of structurally similar compounds. Iniesta et al reported the electrochemical oxidation of phenol on BDD electrodes at 1.67 V vs. SHE in acidic media.<sup>142</sup> The similarity in oxidation potentials between FF and phenol can be rationalised by their comparable aromatic structures and functional groups. This finding suggested that the EBL D-22 electrode successfully facilitated FF oxidation within the potential window -1.2 V to 2.5 V.

Research on FF oxidation using both Pt and Au electrodes instead of BDD electrodes has been previously reported. Pt and Au both have high intrinsic activity for the OER reaction without the need for nanoparticles. Román et al. saw the onset of FF oxidation on Pt electrodes in acidic media between the potentials 0.8 V and 1.45 V before oxygen evolution.<sup>143</sup> A separate research group led by Román found similar results on Au electrodes in acidic media with the onset of FF oxidation occurring between 0.8 V and 1.2 V.<sup>144</sup> This lower potential range in comparison to the EBL D-22 electrode highlights a distinct advantage of metal electrodes in terms of energy efficiency, minimising parasitic oxygen evolution. The inherent chemical inertness and low intrinsic catalytic activity of diamond, where beneficial in other electrochemical applications, proved limiting in this study for FF oxidation when compared to other common noble metal electrodes that have relatively high catalytic activity. Without the presence of additional catalytic species, as was the case in preliminary experiments, only the EBL D-22 electrode exhibited electrochemical activity, highlighting the need for surface modification to enhance reactivity.

Compared to the blank electrolyte (black line in **Fig. 3.9**), an increase in current density was observed for the solution containing FF (red line in **Fig 3.9**) confirming FF oxidation occurred at the electrode surface. This is likely due to the high surface area and enhanced charge transfer properties of EBL-BDD, as tests for f-BDD showed negligent activity for FF oxidation. (**App. 5.4**) The demonstrated activity of EBL D-22 suggests its potential for applications in biomass-derived chemical processing. The high chemical and electrochemical stability and robustness

of the BDD material makes it an excellent candidate for consistent sustainable electrochemical oxidation reactions when combined with an appropriate catalyst.

## 4. Conclusions and Future Work

### 4.1. Conclusions

Many different methods have been explored to optimise the surface area of BDD electrodes for electrochemical applications.<sup>24,27–32,73,137</sup> This thesis successfully demonstrated the fabrication and electrochemical evaluation of nanostructured BDD electrodes prepared via the combination of EBL, RIE, and HFCVD. Through increasing growth times, three electrodes with distinct EBL electrode designs were achieved with appropriate thickness for electrochemical performance as confirmed by SEM imaging and laser Raman spectroscopy. Increased growth time significantly enhanced film thickness, while laser Raman analysis confirmed the successful boron incorporation within the diamond lattice.

Oxygen termination treatments were found to play a crucial role in enhancing the electrochemical activity of the fabricated electrodes. Among the oxygen termination methods tested, ozone treatment (AOZ) was the most effective in enhancing electrochemical properties, achieving the highest  $C_{dl}$  value of  $794.2 \mu\text{F cm}^{-2}$ . This improvement in comparison to a hydrogen terminated electrode was attributed to effective surface oxidation and minimised surface etching in comparison to harsher treatments  $\text{O}_2$  plasma (AOP) and  $\text{H}_2\text{SO}_4$  (AOT), which may have led to partial degradation of the thin BDD films.

Electrochemical characterisation in  $0.1 \text{ M KNO}_3$  revealed that nanostructuring significantly improved electrode performance. The EBL D-05 electrode design, featuring the highest density of nanopillars, exhibited the highest  $C_{dl}$  value of  $794.2 \mu\text{F cm}^{-2}$ , highlighting the direct correlation between nanostructure density and electrochemical surface activity. Additionally, the EBL D-05 electrode exhibited a  $C_{dl}$  value approximately 50 times larger than the average experimental value recorded for the reference f-BDD electrode. Considering that literature-reported values for f-BDD electrodes are often lower than those recorded experimentally in this study, relative comparisons to such references would result in an even more pronounced improvement, thereby further validating the effectiveness of the EBL-BDD electrodes.<sup>35,137</sup> While minor leakage currents were observed in two of the electrode designs, these did not significantly impact overall performance.

Analysis of the electrode surface area reinforced the significant enhancements achieved by nanostructured BDD in comparison to flat BDD.  $S_{\text{Actual}}$  showed a 10.5-fold increase over the f-BDD reference. When considering  $C_{\text{dl}}$  values, the relative effective surface area demonstrated an even greater improvement, with the EBL D-05 electrode exhibiting a 25.4-fold increase compared to f-BDD. This underscores the importance of physically structuring as well as the electrochemical accessibility of the electrode surfaces.

Preliminary FF oxidation trials indicated the potential for EBL-BDD electrodes to be used in biomass-derived chemical processing. The EBL D-22 electrode demonstrated clear electrochemical activity toward FF oxidation, exhibiting an anodic peak at 1.6 V vs. Ag/AgCl, aligning closely with literature reports for structurally similar compounds.<sup>141,142</sup> The oxidation potential was higher than that observed for noble metal electrodes suggesting decreased efficiency of the EBL-BDD electrode in comparison.<sup>143,144</sup> However, this initial result reflected the catalytic promise of the EBL-BDD electrode, particularly when considering future integration of nanoparticle catalysts.

## 4.2. Future Work

This study has demonstrated a relatively novel approach to increasing the surface area of BDD electrodes for electrochemical applications. Building upon these findings, several aspects of further investigation can be proposed to expand and refine the understanding of EBL-BDD electrochemical performance. In particular, future work should focus on evaluating additional electrochemical characteristics. To explore the potential for electrochemical sensing applications, further experiments using an electrolyte solution containing a standard redox probe, such as KCl with  $[\text{Ru}(\text{NH}_3)_6]^{3+}$ , are recommended. Comparison of the resulting peak currents across each electrode design will provide insight into the relative electroactive surface areas and the effectiveness of the EBL nanostructuring approach. Peak separation ( $\Delta E_p$ ) might also be examined to give insight into electron transfer kinetics. Single-crystal BDD electrodes have exhibited near-reversible redox behaviour, therefore investigations of nanostructured polycrystalline BDD electrodes could be particularly interesting.<sup>145</sup> Further investigations should be conducted to assess the stability of the electrodes developed in this work. Varying the scan rate during CV testing would be useful to provide insights into the surface stability of the electrodes. The point of electrode degradation could be identified based on reductions in

peak currents or distortion of peak profiles. Long-term tests of multiple cycles would be beneficial to indicate long-term stability over extended operational periods.<sup>146</sup> Such testing would determine the suitability of EBL-BDD electrodes for industrial applications.

In terms of understanding the electrode surface morphology, additional imaging techniques should be employed to provide greater knowledge of the nanostructured features, the distribution of B within the diamond lattice, and the uniformity of diamond film coverage prior to CV testing. Atomic force microscopy (AFM) would give a high-resolution 3D topography of the BDD surface and combined with SEM can measure roughness with precision down to the nanoscale to properly observe the nanopillars of the EBL-BDD designs.<sup>128</sup> Secondary ion mass spectrometry (SIMS) is highly sensitive to light elements such as B and could provide depth profiling of the B distribution throughout the BDD film.<sup>127</sup>

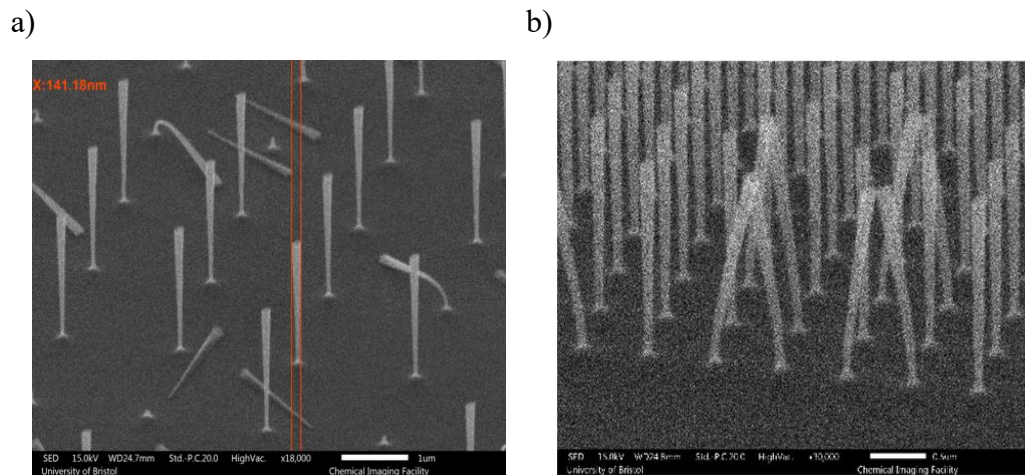
The problems encountered during the BDD film deposition process should also be addressed, particularly the need for multiple sequential depositions using the HFCVD system. Issues such as variability in film quality and the potential introduction of defects between deposition sessions should be carefully investigated to enhance reproducibility across the same electrode designs. Additionally, greater attention should be directed towards mitigating leaking current, as evidenced by the ohmic behaviour in the CV profiles of the EBL D-22 and the EBL D-05 electrodes presented in **Figure 3.5**. Proper sealing of the electrode holder and performing leak tests in ultrapure water before addition of the electrolyte should be done to identify leaking sources. Additionally, ensuring only the working electrode surface is exposed to the electrolyte and not the conductive Si base to avoid stray current paths is essential. Finally, iR compensation should be used via the potentiostat to reduce slanted baselines from solution resistance.

For future work in FF oxidation, the confirmation of catalytic activity by the observed anodic peak at 1.67 vs. Ag/AgCl provides a foundation for further surface modifications to reduce the onset potential and improve energy efficiency for commercial use. The enhancement of BDD electrode catalytic activity through nanoparticle decoration has been successfully explored in prior studies.<sup>100</sup> Furthermore, the high OER potentials characteristic of BDD electrodes are advantageous for electro-oxidation reactions, as it enables the generation of more OH radicals at the anode surface, thereby enhancing the oxidative capacity of the electrode compared to conventional electrodes.<sup>147</sup> Building on these factors, future tests for FF oxidation should incorporate the decoration of nanoparticles, such as CuO and ZnO, to achieve electrochemical

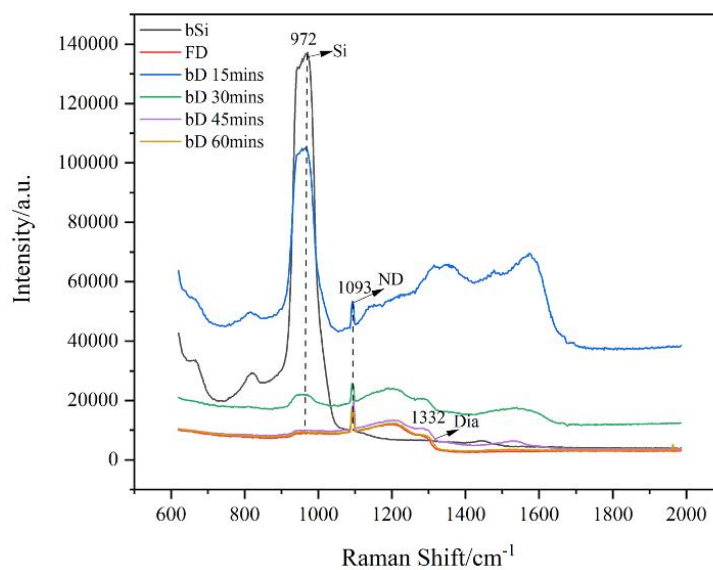
activity for all electrode designs in this work. Metal deposition by way of Ni-Cu alloy is an alternative method to increase catalytic activity on the BDD surface and both the EBL D-22 and EBL D-15 electrodes with larger pitches would be particularly suitable for this approach. Ni particles would also interact with BDD to form a porous structure increasing surface area further.<sup>148</sup> Additionally, subsequent bulk electrolysis experiments to assess the performance of EBL-BDD electrodes in the selective valorisation of FF should be conducted, with the aim of producing desired high-value products efficiently and sustainably. These results can then be transferred to work in water splitting.

This research has demonstrated that rational design and surface modification of BDD electrodes can significantly influence their electrochemical performance. The insights gained from this study provide a strong foundation for future advancements in BDD technology, specifically using HFCVD in conjunction with EBL programming. Potential applications include the oxidation of FF and water splitting for sustainable fuel production as well as organic pollutant degradation and electrochemical sensing. By continuing to refine electrode structures, surface treatments, and scalability, BDD electrodes can be further optimised for a wide range of electrochemical applications.

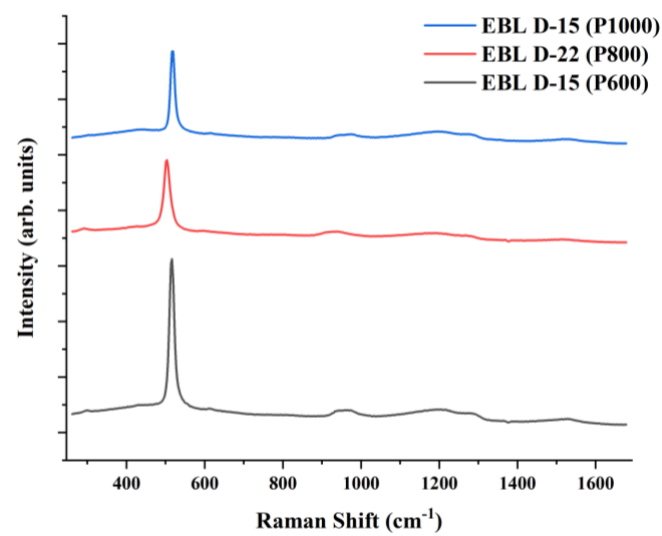
## 5. Appendix



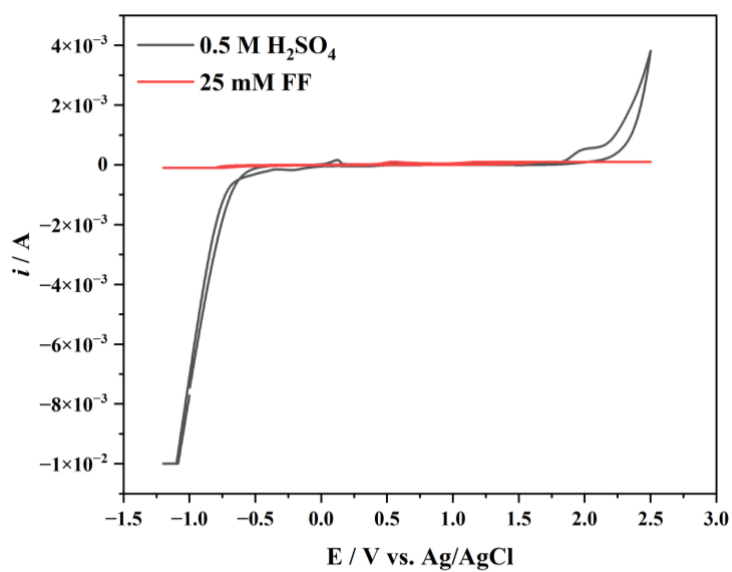
5.1.1. SEM images of EBL-Si with a) thickness ( $T$ )  $< 200$  nm and b) pitch ( $P$ )  $< 500$  nm.



5.2. Visible laser Raman spectra for black diamond (bD) electrodes fabricated for different growth times from 15-60 minutes.



5.3. Visible Laser Raman spectra for each EBL-BDD electrode showing a significant first-order Si peak.



5.4. CV of 0.5 M H<sub>2</sub>SO<sub>4</sub> and 0.5 M H<sub>2</sub>SO<sub>4</sub> + 25 mM FF,  $\nu = 100 \text{ mV s}^{-1}$  with EBL D-22

## 6. References

- 1 M. Hupert, A. Muck, J. Wang, J. Stotter, Z. Cvackova, S. Haymond, Y. Show and G. M. Swain, *Diam Relat Mater*, 2003, **12**, 1940–1949.
- 2 S. R. Belding, F. W. Campbell, E. J. F. Dickinson and R. G. Compton, *Physical Chemistry Chemical Physics*, 2010, **12**, 11208–11221.
- 3 C. V RAMAN, *Curr Sci*, 1943, **12**, 33–42.
- 4 K. Miyoshi, 2019, pp. 333–354.
- 5 B. D. Cullity, in *Elements of X-Ray Diffraction*, Addison-Wesley Publishing, Reading, MA, 1956, pp. 29–60.
- 6 W. J. P. van Enckevort, G. Janssen and L. J. Giling, *J Cryst Growth*, 1991, **113**, 295–304.
- 7 Ch. Wild, N. Herres and P. Koidl, *J Appl Phys*, 1990, **68**, 973–978.
- 8 G. Janssen, J. J. Schermer, W. J. P. van Enckevort and L. J. Giling, *J Cryst Growth*, 1992, **125**, 42–50.
- 9 Z. Shpilman, I. Gouzman, E. Grossman, L. Shen, T. K. Minton, J. T. Paci, G. C. Schatz, R. Akhvlediani and A. Hoffman, *The Journal of Physical Chemistry C*, 2010, **114**, 18996–19003.
- 10 L. Celbová, P. Ashcheulov, L. Klimša, J. Kopeček, K. Aubrechtová Dragounová, J. Luštinec, J. Macák, R. Škoda and I. Kratochvílová, *Materials*, DOI:10.3390/ma14216315.
- 11 P. Puthongkham and B. J. Venton, *ACS Sens*, 2019, **4**, 2403–2411.
- 12 H. Yang, Y. Ma and Y. Dai, *Functional Diamond*, 2022, **1**, 150–159.
- 13 Y. Einaga, *J Appl Electrochem*, 2010, **40**, 1807–1816.
- 14 C. Kittel, in *Introduction to Solid State Physics*, ed. S. Johnson, John Wiley & Sons, Inc, Berkeley, 8th edn., 2005, pp. 187–191.
- 15 C. Kittel, in *Introduction to Solid State Physics*, John Wiley & Sons, Hoboken, New Jersey, 8th edn., 2005, pp. 173–200.
- 16 P. Capper, in *Narrow-gap II-VI Compounds for Optoelectronic and Electromagnetic Applications*, ed. P. Capper, Springer US, 1997, vol. 3, pp. 211–212.
- 17 S. K. Haram, in *Handbook of Electrochemistry*, ed. C. G. Zoski, Elsevier, Amsterdam, 2007, pp. 329–389.
- 18 I. G. Austin and R. Wolfe, *Proceedings of the Physical Society. Section B*, 1956, **69**, 329.
- 19 E. P. Visser, G. J. Bauhuis, G. Janssen, W. Vollenberg, J. P. van Enckevort and L. J. Giling, *Journal of Physics: Condensed Matter*, 1992, **4**, 7365.
- 20 K. Nishimura, K. Das and J. T. Glass, *J Appl Phys*, 1991, **69**, 3142–3148.
- 21 Yu. V Pleskov, *Russian Journal of Electrochemistry*, 2002, **38**, 1275–1291.
- 22 P. Wurzinger, P. Pongratz, P. Hartmann, R. Haubner and B. Lux, *Diam Relat Mater*, 1997, **6**, 763–768.
- 23 Y. Gong, W. Jia, B. Zhou, K. Zheng, J. Gao, Y. Wu, Y. Wang, S. Yu, Y. Xue and Y. Wu, *Appl Surf Sci*, 2024, **659**, 159838.
- 24 F. Gao and C. E. Nebel, in *Nanocarbons for Electroanalysis*, John Wiley & Sons, Ltd, 2017, pp. 197–226.
- 25 N. Hosokawa, R. Matsuzaki and T. Asamaki, *Jpn J Appl Phys*, 1974, **13**, 435.
- 26 H. S. Hiromu Shiomi, *Jpn J Appl Phys*, 1997, **36**, 7745.
- 27 W. Smirnov, A. Kriele, N. Yang and C. E. Nebel, *Diam Relat Mater*, 2010, **19**, 186–189.
- 28 S. Szunerits, Y. Coffinier, E. Galopin, J. Brenner and R. Boukherroub, *Electrochem commun*, 2010, **12**, 438–441.
- 29 C. E. Nebel, N. Yang, H. Uetsuka, E. Osawa, N. Tokuda and O. Williams, *Diam Relat Mater*, 2009, **18**, 910–917.
- 30 J. Zhang, Z. Zhao, Z. Zhang, J. Pei, X. Yu, Y. Coffinier, S. Szunerits, R. Boukherroub and C. Yang, *Electrochim Acta*, 2022, **421**, 140500.
- 31 Y. Zou, P. W. May, S. M. C. Vieira and N. A. Fox, *J Appl Phys*, 2012, **112**, 044903.
- 32 H. Zanin, P. W. May, D. J. Fermin, D. Plana, S. M. C. Vieira, W. I. Milne and E. J. Corat, *ACS Appl Mater Interfaces*, 2014, **6**, 990–995.
- 33 Y. Liu, B. B. Coxon, M. Patena, B. Hoey, J. M. Cole and D. J. Gray, *Energy*

- 115 Z.-H. Jin, D. Yu, Y.-X. Liu, Z.-Y. Tian, S. Richter, M. Braun-Unkhoff, C. Naumann and J.-Z. Yang, *Combust Flame*, 2021, **226**, 200–210.
- 116 P. Zhu, M. Shi, Z. Shen, X. Liao and Y. Chen, *Chem Sci*, 2024, **15**, 4723–4756.
- 117 G. M. Swain, *J Electrochem Soc*, 1994, **141**, 3382.
- 118 F. Liu, Z. Deng, D. Miao, W. Chen, Y. Wang, K. Zhou, L. Ma and Q. Wei, *J Environ Chem Eng*, 2021, **9**, 106369.
- 119 A. Zazoua, K. Nawal and N. and Jaffrezic-Renault, *Anal Lett*, 2018, **51**, 336–347.
- 120 A. Manivannan, S. M. S., T. D. A. and A. and Fujishima, *Anal Lett*, 2002, **35**, 355–368.
- 121 I. N. Rizki, B. Y. Wardhana, L. G. Sutanto and P. K. Jiwanti, *AIP Conf Proc*, 2024, **3047**, 050003.
- 122 M. Carolyne Prete, L. Rianne da Rocha, M. Gava Segatelli, R. Antigo Medeiros, G. M. Swain and C. R. T. Tarley, *Electroanalysis*, 2025, **37**, e202400121.
- 123 K. Jackowska and P. Krysinski, *Anal Bioanal Chem*, 2013, **405**, 3753–3771.
- 124 A. Lytvynenko, S. Baluchová, J. Zima, J. Krusek and K. Peckova, *Bioelectrochemistry*, 2024, **158**, 108713.
- 125 P. Pinar, Y. Yardim and Z. Senturk, *Diam Relat Mater*, 2019, **101**, 107649.
- 126 H. Long, H. Hu, K. Wen, X. Liu, S. Liu, Q. Zhang and T. Chen, *Molecules*, DOI:10.3390/molecules28062829.
- 127 P. W. May, W. J. Ludlow, M. Hannaway, P. J. Heard, J. A. Smith and K. N. Rosser, *Chem Phys Lett*, 2007, **446**, 103–108.
- 128 D. K. Simon, M. Tsigkourakos, T. Hantschel, T. Conard and W. Vandervorst, *physica status solidi (a)*, 2013, **210**, 2002–2007.
- 129 J. Yu, R. fang Huang, L. Wen and C. Shi, *Mater Res Bull*, 1999, **34**, 2319–2325.
- 130 K. Ushizawa, K. Watanabe, T. Ando, I. Sakaguchi, M. Nishitani-Gamo, Y. Sato and H. Kanda, *Diam Relat Mater*, 1998, **7**, 1719–1722.
- 131 F. Cerdeira, T. A. Fjeldly and M. Cardona, *Phys Rev B*, 1973, **8**, 4734–4745.
- 132 L. Bergman and R. J. Nemanich, *J Appl Phys*, 1995, **78**, 6709–6719.
- 133 I. Duo, C. Levy-Clement, A. Fujishima and C. Comninellis, *J Appl Electrochem*, 2004, **34**, 935–943.
- 134 D. Liu, L. Gou, J. Xu, K. Gao and X. Kang, *Vacuum*, 2016, **128**, 80–84.
- 135 W. Zhang, Z.-H. Huang, G. Cao, F. Kang and Y. Yang, *J Power Sources*, 2012, **204**, 230–235.
- 136 S. Suman, D. K. Sharma, O. Szabo, B. Rakesh, M. Marton, M. Vojs, A. Vincze, S. P. Dutta, U. Balaji, D. Debasish, R. Sakthivel, K. J. Sankaran and A. Kromka, *J. Mater. Chem. A*, 2024, **12**, 21134–21147.
- 137 P. Knittel, F. Buchner, E. Hadzifejzovic, C. Giese, P. Quellmalz, R. Seidel, T. Petit, B. Iliev, T. J. S. Schubert, C. E. Nebel and J. S. Foord, *ChemCatChem*, 2020, **12**, 5548–5557.
- 138 S. Baluchová, A. Taylor, V. Mortet, S. Sedláková, L. Klimša, J. Kopeček, O. Hák and K. Schwarzová-Pecková, *Electrochim Acta*, 2019, **327**, 135025.
- 139 K. Xia, Q. Gao, J. Jiang and J. Hu, *Carbon N Y*, 2008, **46**, 1718–1726.
- 140 T. Kondo, Y. Kodama, S. Ikezoe, K. Yajima, T. Aikawa and M. Yuasa, *Carbon N Y*, 2014, **77**, 783–789.
- 141 C.-H. Lee, E.-S. Lee, Y.-K. Lim, K.-H. Park, H.-D. Park and D.-S. Lim, *RSC Adv*, 2017, **7**, 6229–6235.
- 142 J. Iniesta, P. A. Michaud, M. Panizza, G. Cerisola, A. Aldaz and Ch. Comninellis, *Electrochim Acta*, 2001, **46**, 3573–3578.
- 143 A. M. Román, J. C. Hasse, J. W. Medlin and A. Holewinski, *ACS Catal*, 2019, **9**, 10305–10316.
- 144 A. M. Román, N. Agrawal, J. C. Hasse, M. J. Janik, J. W. Medlin and A. Holewinski, *J Catal*, 2020, **391**, 327–335.
- 145 Z. Liu, S. Baluchová, A. F. Sartori, Z. Li, Y. Gonzalez-Garcia, M. Schreck and J. C. Ruinero, *Carbon N Y*, 2023, **201**, 1229–1240.

- 1 M. Hupert, A. Muck, J. Wang, J. Stotter, Z. Cvackova, S. Haymond, Y. Show and G. M. Swain, *Diam Relat Mater*, 2003, **12**, 1940–1949.
- 2 S. R. Belding, F. W. Campbell, E. J. F. Dickinson and R. G. Compton, *Physical Chemistry Chemical Physics*, 2010, **12**, 11208–11221.
- 3 C. V RAMAN, *Curr Sci*, 1943, **12**, 33–42.
- 4 K. Miyoshi, 2019, pp. 333–354.
- 5 B. D. Cullity, in *Elements of X-Ray Diffraction*, Addison-Wesley Publishing, Reading, MA, 1956, pp. 29–60.
- 6 W. J. P. van Enckevort, G. Janssen and L. J. Giling, *J Cryst Growth*, 1991, **113**, 295–304.
- 7 Ch. Wild, N. Herres and P. Koidl, *J Appl Phys*, 1990, **68**, 973–978.
- 8 G. Janssen, J. J. Schermer, W. J. P. van Enckevort and L. J. Giling, *J Cryst Growth*, 1992, **125**, 42–50.
- 9 Z. Shpilman, I. Gouzman, E. Grossman, L. Shen, T. K. Minton, J. T. Paci, G. C. Schatz, R. Akhvlediani and A. Hoffman, *The Journal of Physical Chemistry C*, 2010, **114**, 18996–19003.
- 10 L. Celbová, P. Ashcheulov, L. Klimša, J. Kopeček, K. Aubrechtová Dragounová, J. Luštinec, J. Macák, R. Škoda and I. Kratochvílová, *Materials*, 2021, **14**, 6315.
- 11 P. Puthongkham and B. J. Venton, *ACS Sens*, 2019, **4**, 2403–2411.
- 12 H. Yang, Y. Ma and Y. Dai, *Functional Diamond*, 2022, **1**, 150–159.
- 13 Y. Einaga, *J Appl Electrochem*, 2010, **40**, 1807–1816.
- 14 C. Kittel, in *Introduction to Solid State Physics*, ed. S. Johnson, John Wiley & Sons, Inc, Berkeley, 8th edn., 2005, pp. 187–191.
- 15 C. Kittel, in *Introduction to Solid State Physics*, John Wiley & Sons, Hoboken, New Jersey, 8th edn., 2005, pp. 173–200.
- 16 P. Capper, in *Narrow-gap II-VI Compounds for Optoelectronic and Electromagnetic Applications*, ed. P. Capper, Springer US, 1997, vol. 3, pp. 211–212.
- 17 S. K. Haram, in *Handbook of Electrochemistry*, ed. C. G. Zoski, Elsevier, Amsterdam, 2007, pp. 329–389.
- 18 I. G. Austin and R. Wolfe, *Proceedings of the Physical Society. Section B*, 1956, **69**, 329.
- 19 E. P. Visser, G. J. Bauhuis, G. Janssen, W. Vollenberg, J. P. van Enckevort and L. J. Giling, *Journal of Physics: Condensed Matter*, 1992, **4**, 7365.
- 20 K. Nishimura, K. Das and J. T. Glass, *J Appl Phys*, 1991, **69**, 3142–3148.
- 21 Yu. V Pleskov, *Russian Journal of Electrochemistry*, 2002, **38**, 1275–1291.
- 22 P. Wurzinger, P. Pongratz, P. Hartmann, R. Haubner and B. Lux, *Diam Relat Mater*, 1997, **6**, 763–768.
- 23 Y. Gong, W. Jia, B. Zhou, K. Zheng, J. Gao, Y. Wu, Y. Wang, S. Yu, Y. Xue and Y. Wu, *Appl Surf Sci*, 2024, **659**, 159838.
- 24 F. Gao and C. E. Nebel, in *Nanocarbons for Electroanalysis*, John Wiley & Sons, Ltd, 2017, pp. 197–226.
- 25 N. Hosokawa, R. Matsuzaki and T. Asamaki, *Jpn J Appl Phys*, 1974, **13**, 435.
- 26 H. S. Hiromu Shiomi, *Jpn J Appl Phys*, 1997, **36**, 7745.
- 27 W. Smirnov, A. Kriele, N. Yang and C. E. Nebel, *Diam Relat Mater*, 2010, **19**, 186–189.
- 28
- 28 S. Szunerits, Y. Coffinier, E. Galopin, J. Brenner and R. Boukherroub, *Electrochem commun*, 2010, **12**, 438–441.

- 29 C. E. Nebel, N. Yang, H. Uetsuka, E. Osawa, N. Tokuda and O. Williams, *Diam Relat Mater*, 2009, **18**, 910–917.
- 30 J. Zhang, Z. Zhao, Z. Zhang, J. Pei, X. Yu, Y. Coffinier, S. Szunerits, R. Boukherroub and C. Yang, *Electrochim Acta*, 2022, **421**, 140500.
- 31 Y. Zou, P. W. May, S. M. C. Vieira and N. A. Fox, *J Appl Phys*, 2012, **112**, 044903.
- 32 H. Zanin, P. W. May, D. J. Fermin, D. Plana, S. M. C. Vieira, W. I. Milne and E. J. Corat, *ACS Appl Mater Interfaces*, 2014, **6**, 990–995.
- 33 X. Liu, P. R. Coxon, M. Peters, B. Hoex, J. M. Cole and D. J. Fray, *Energy Environ Sci*, 2014, **7**, 3223–3263.
- 34 H. Jansen, M. de Boer, R. Legtenberg and M. Elwenspoek, *Journal of Micromechanics and Microengineering*, 1995, **5**, 115.
- 35 P. W. May, M. Clegg, T. A. Silva, H. Zanin, O. Fatibello-Filho, V. Celorrio, D. J. Fermin, C. C. Welch, G. Hazell, L. Fisher, A. Nobbs and B. Su, *J. Mater. Chem. B*, 2016, **4**, 5737–5746.
- 36 T. H. P. Chang and W. C. Nixon, *Solid State Electron*, 1967, **10**, 701–704.
- 37 A. Tseng, K. Chen, C. Chen and M. Kung Jeng, *Electronics Packaging Manufacturing, IEEE Transactions on*, 2003, **26**, 141–149.
- 38 E. Sharma, R. Rath, J. Misharwal, B. Sinhmar, S. Kumari, J. Dalal and A. Kumar, *Nanomaterials*, 2022, **12**, 2754.
- 39 S. Grigoropoulos, E. Gogolides, A. Tserepi and A. Nassiopoulou, *Journal of Vacuum Science & Technology B: Microelectronics and Nanometer Structures*, 1997, **15**, 640–645.
- 40 C. Gatzert, A. W. Blakers, P. N. K. Deenapanray, D. Macdonald and F. D. Auret, *Journal of Vacuum Science & Technology A*, 2006, **24**, 1857–1865.
- 41 V.-C. Su, C. H. Chu, G. Sun and D. P. Tsai, *Opt Express*, 2018, **26**, 13148–13182.
- 42 A. K. C., R. Saha, J. Anderson, A. Ayala, C. Engdahl, E. L. Piner and M. W. Holtz, *J Appl Phys*, 2021, **130**, 225302.
- 43 J. C. Arnault and H. A. Girard, *Nanodiamond*, R. S. of Chemistry and O. A. Williams, The Royal Society of Chemistry, Cambridge, 2014.
- 44 N. Jiang, B. W. Sun, Z. Zhang and Z. Lin, *J Mater Res*, 1994, **9**, 2695–2702.
- 45 O. A. Williams, O. Douhéret, M. Daenen, K. Haenen, E. Osawa and M. Takahashi, *Chem Phys Lett*, 2007, **445**, 255–258.
- 46 Y. Matsushima, Y. Nemoto, T. Yamazaki, K. Maeda and T. Suzuki, *Sens Actuators B Chem*, 2003, **96**, 133–138.
- 47 A. P. Malshe, R. A. Beera, A. A. Khanolkar, W. D. Brown and H. A. Naseem, *Diam Relat Mater*, 1997, **6**, 430–434.
- 48 F. P. Bundy, H. T. Hall, H. M. Strong and R. H. Wentorfjun., *Nature*, 1955, **176**, 51–55.
- 49 United States Patent Office, 3030188, 1962.
- 50 M. Frenklach and K. E. Spear, *J Mater Res*, 1988, **3**, 133–140.
- 51 W. A. Yarborough, in *Materials Science Monographs*, eds. Y. Tzeng, M. Yoshikawa, M. Murakawa and A. Feldman, Elsevier, 1991, vol. 73, pp. 25–34.
- 52 M. Hiramatsu, K. Kato, C. H. Lau, J. S. Foord and M. Hori, *Diam Relat Mater*, 2003, **12**, 365–368.
- 53 P. W. May and Y. A. Mankelevich, *The Journal of Physical Chemistry C*, 2008, **112**, 12432–12441.
- 54 J. C. Angus, *Diam Relat Mater*, 2014, **49**, 77–86.
- 55 D. V Fedoseev, K. S. Uspenskaya, V. P. Varnin and S. P. Vnukov, *Bulletin of the Academy of Sciences of the USSR, Division of chemical science*, 1978, **27**, 1088–1091.
- 56 J. J. Gracio, Q. H. Fan and J. C. Madaleno, *J Phys D Appl Phys*, 2010, **43**, 374017.

- 57 H. O. Pierson, in *Handbook of Carbon, Graphite, Diamonds and Fullerenes*, ed. H. O. Pierson, William Andrew Publishing, Oxford, 1993, pp. 302–336.
- 58 P. W. May, N. M. Everitt, C. G. Trevor, M. N. R. Ashfold and K. N. Rosser, *Appl Surf Sci*, 1993, **68**, 299–305.
- 59 N. Khelef, F. Khelfaoui and O. Babahani, *Journal of Engineering and Applied Science*, 2022, **69**, 73.
- 60 S. J. Harris, J. Kiefer, Q. Zhang, A. Schoene and K. Lee, *J Electrochem Soc*, 1998, **145**, 3203.
- 61 V. V. S. S. Srikanth and X. Jiang, in *Synthetic Diamond Films: Preparation, Electrochemistry, Characterization, and Applications*, eds. E. Brillias and C. A. Martínez-Huitle, John Wiley & Sons, Inc., 2011, pp. 21–55.
- 62 K. W. Hemawan and R. J. Hemley, *Journal of Vacuum Science & Technology A*, 2015, **33**, 061302.
- 63 M. Kamo, Y. Sato, S. Matsumoto and N. Setaka, *J Cryst Growth*, 1983, **62**, 642–644.
- 64 S.-T. Lee, Z. Lin and X. Jiang, *Materials Science and Engineering: R: Reports*, 1999, **25**, 123–154.
- 65 P. K. Bachmann, H. J. Hagemann, H. Lade, D. Leers, D. U. Wiechert, H. Wilson, D. Fournier and K. Plamann, *Diam Relat Mater*, 1995, **4**, 820–826.
- 66 M. Werner and R. Locher, *Reports on Progress in Physics*, 1998, **61**, 1665.
- 67 J. Weng, F. Liu, L. W. Xiong, J. H. Wang and Q. Sun, *Vacuum*, 2018, **147**, 134–142.
- 68 S. Matsumoto, Y. Sato, M. Kamo and N. Setaka, *Jpn J Appl Phys*, 1982, **21**, L183.
- 69 United States Patent, 3623712, 1971.
- 70 United States Patent, 4047496, 1977.
- 71 S. P. Chauhan, J. C. Angus and N. C. Gardner, *J Appl Phys*, 1976, **47**, 4746–4754.
- 72 J. M. T. Thompson and P. W. May, *Philosophical Transactions of the Royal Society of London. Series A: Mathematical, Physical and Engineering Sciences*, 2000, **358**, 473–495.
- 73 B. C. Lourencao, T. A. Silva, H. Zanin, P. W. May, E. J. Corat and O. Fatibello-Filho, *Journal of Solid State Electrochemistry*, 2016, **20**, 2403–2409.
- 74 S. Kim, Y. Jeong, M.-O. Park, Y. Jang, J.-S. Bae, K.-S. Hong, S. Kim, P. Song and J.-H. Yoon, *Journal of Materials Research and Technology*, 2023, **23**, 1375–1385.
- 75 S. Ohmagari, *Functional Diamond*, 2023, **3**, 2259941.
- 76 Y. Takamori, M. Nagai, T. Tabakoya, Y. Nakamura, S. Yamasaki, C. E. Nebel, X. Zhang, T. Matsumoto, T. Inokuma and N. Tokuda, *Diam Relat Mater*, 2021, **118**, 108515.
- 77 A. Abdullah and A. Mohammed, presented in part at The International Conference on Hydraulics, Pneumatics, Sealing Elements, Precision Mechanics, Tools, Specific Electronic Equipment & Mechatronics, Baile Govora, November, 2018
- 78 T. E. Davies, H. Li, S. Bessette, R. Gauvin, G. S. Patience and N. F. Dummer, *Can J Chem Eng*, 2022, **100**, 3145–3159.
- 79 S. Praver and R. J. Nemanich, *Philosophical Transactions of the Royal Society of London. Series A: Mathematical, Physical and Engineering Sciences*, 2004, **362**, 2537–2565.
- 80 A. C. Ferrari and J. Robertson, *Phys Rev B*, 2000, **61**, 14095–14107.
- 81 J. Filik, J. N. Harvey, N. L. Allan, P. W. May, J. E. P. Dahl, S. Liu and R. M. K. Carlson, *Phys Rev B*, 2006, **74**, 35423.
- 82

82. A. J. Bard and L. R. Faulkner, in *Electrochemical methods: fundamentals and applications*, eds. A. J. Bard and L. R. Faulkner, John Wiley & Sons, Inc., Hoboken, NJ, 2nd edn., 2001, pp. 13–13.
83. C. Breitkopf and K. Swider-Lyons, *Springer Handbook of Electrochemical Energy*, Springer Berlin, Heidelberg, Germany, 2016.
84. M. Ciobanu, J. P. Wilburn, M. L. Krim and D. E. Cliffel, in *Handbook of Electrochemistry*, ed. C. G. Zoski, Elsevier, Amsterdam, 2007, pp. 3–29.
85. D. Shi, L. Liu, Z. Zhai, B. Chen, Z. Lu, C. Zhang, Z. Yuan, M. Zhou, B. Yang, N. Huang and X. Jiang, *J Mater Sci Technol*, 2021, **86**, 1–10.
86. I. Yagi, H. Notsu, T. Kondo, D. A. Tryk and A. Fujishima, *Journal of Electroanalytical Chemistry*, 1999, **473**, 173–178.
87. T. Sakai, K.-S. Song, H. Kanazawa, Y. Nakamura, H. Umezawa, M. Tachiki and H. Kawarada, *Diam Relat Mater*, 2003, **12**, 1971–1975.
88. F. B. Liu, J. D. Wang, B. Liu, X. M. Li and D. R. Chen, *Diam Relat Mater*, 2007, **16**, 454–460.
89. A. Denisenko, C. Pietzka, A. Romanyuk, H. El-Hajj and E. Kohn, *J Appl Phys*, 2008, **103**, 014904.
90. J. Scharpf, A. Denisenko, C. Pietzka and E. Kohn, *Diam Relat Mater*, 2011, **20**, 1250–1254.
91. Y. Yao, C. Ma, J. Wang, W. Qiao, L. Ling and D. Long, *ACS Appl Mater Interfaces*, 2015, **7**, 4817–4825.
92. H. Yamada, H. Nakamura, F. Nakahara, I. Moriguchi and T. Kudo, *The Journal of Physical Chemistry C*, 2007, **111**, 227–233.
93. S. Zhang, S. Gao, H. Dong, X. Wang, M. Liu, Y. Sun, X. Wu, J. Xu, L. Chen, A. Yuan and W. Lu, *Journal of Electroanalytical Chemistry*, 2019, **840**, 423–429.
94. A. Otake, T. Nishida, S. Ohmagari and Y. Einaga, *JACS Au*, 2024, **4**, 1184–1193.
95. International Energy Agency, *World Energy Outlook 2024*, Paris, 2024.
96. E. Skúlason, G. S. Karlberg, J. Rossmeisl, T. Bligaard, J. Greeley, H. Jónsson and J. K. Nørskov, *Physical Chemistry Chemical Physics*, 2007, **9**, 3241–3250.
97. M. Đurovič, J. Hnát and K. Bouzek, *J Power Sources*, 2021, **493**, 229708.
98. S. Wang, A. Lu and C.-J. Zhong, *Nano Converge*, 2021, **8**, 4.
99. I. Gerger, R. Haubner, H. Kronberger and G. Fafilek, *Diam Relat Mater*, 2004, **13**, 1062–1069.
100. Y. Al-Abdallat, I. Jumah, R. Jumah, H. Ghanem and A. Telfah, *Energies (Basel)*, 2020, **13**, 5264.
101. T. Zhang, W. Li, H. Xiao, Y. Jin and S. Wu, *Bioresour Technol*, 2022, **354**, 127126.
102. D. Edumujeze, M.-C. Fournier-Salaün and S. Leveneur, *Fuel*, 2025, **381**, 133423.
103. C.-H. Zhou, X. Xia, C.-X. Lin, D.-S. Tong and J. Beltramini, *Chem Soc Rev*, 2011, **40**, 5588–5617.
104. F. H. Isikgor and C. R. Becer, *Polym Chem*, 2015, **6**, 4497–4559.
105. X. Zhang, S. Xu, Q. Li, G. Zhou and H. Xia, *RSC Adv*, 2021, **11**, 27042–27058.
106. F. Drault, Y. Snoussi, S. Paul, I. Itabaiana Jr. and R. Wojcieszak, *ChemSusChem*, 2020, **13**, 5164–5172.
107. X. Li, B. Ho, D. S. W. Lim and Y. Zhang, *Green Chemistry*, 2017, **19**, 914–918.
108. R. Wojcieszak, F. Santarelli, S. Paul, F. Dumeignil, F. Cavani and R. V Gonçalves, *Sustainable Chemical Processes*, 2015, **3**, 9.
109. R. Mariscal, P. Maireles-Torres, M. Ojeda, I. Sádaba and M. López Granados, *Energy Environ Sci*, 2016, **9**, 1144–1189.
110. B. Chen, F. Li and G. Yuan, *RSC Adv*, 2017, **7**, 21145–21152.

- 111 A. Lolli, S. Albonetti, L. Utili, R. Amadori, F. Ospitali, C. Lucarelli and F. Cavani, *Appl Catal A Gen*, 2015, **504**, 408–419.
- 112 S. Zhang, J. Lan, Z. Chen, G. Yin and G. Li, *ACS Sustain Chem Eng*, 2017, **5**, 9360–9369.
- 113 H. Zhou, H. Xu, X. Wang and Y. Liu, *Green Chemistry*, 2019, **21**, 2923–2927.
- 114 A. Banerjee, G. R. Dick, T. Yoshino and M. W. Kanan, *Nature*, 2016, **531**, 215–219.
- 115 Z.-H. Jin, D. Yu, Y.-X. Liu, Z.-Y. Tian, S. Richter, M. Braun-Unkhoff, C. Naumann and J.-Z. Yang, *Combust Flame*, 2021, **226**, 200–210.
- 116 P. Zhu, M. Shi, Z. Shen, X. Liao and Y. Chen, *Chem Sci*, 2024, **15**, 4723–4756.
- 117 G. M. Swain, *J Electrochem Soc*, 1994, **141**, 3382.
- 118 F. Liu, Z. Deng, D. Miao, W. Chen, Y. Wang, K. Zhou, L. Ma and Q. Wei, *J Environ Chem Eng*, 2021, **9**, 106369.
- 119 A. Zazoua, K. Nawal and N. and Jaffrezic-Renault, *Anal Lett*, 2018, **51**, 336–347.
- 120 A. Manivannan, S. M. S., T. D. A. and A. and Fujishima, *Anal Lett*, 2002, **35**, 355–368.
- 121 I. N. Rizki, B. Y. Wardhana, L. G. Sutanto and P. K. Jiwanti, *AIP Conf Proc*, 2024, **3047**, 050003.
- 122 M. Carolyne Prete, L. Rianne da Rocha, M. Gava Segatelli, R. Antigo Medeiros, G. M. Swain and C. R. T. Tarley, *Electroanalysis*, 2025, **37**, e202400121.
- 123 K. Jackowska and P. Kryszynski, *Anal Bioanal Chem*, 2013, **405**, 3753–3771.
- 124 A. Lytvynenko, S. Baluchová, J. Zima, J. Krusek and K. Peckova, *Bioelectrochemistry*, 2024, **158**, 108713.
- 125 P. Pinar, Y. Yardim and Z. Senturk, *Diam Relat Mater*, 2019, **101**, 107649.
- 126 H. Long, H. Hu, K. Wen, X. Liu, S. Liu, Q. Zhang and T. Chen, *Molecules*, 2023, **28**, 2829.
- 127 P. W. May, W. J. Ludlow, M. Hannaway, P. J. Heard, J. A. Smith and K. N. Rosser, *Chem Phys Lett*, 2007, **446**, 103–108.
- 128 D. K. Simon, M. Tsigkourakos, T. Hantschel, T. Conard and W. Vandervorst, *physica status solidi (a)*, 2013, **210**, 2002–2007.
- 129 J. Yu, R. fang Huang, L. Wen and C. Shi, *Mater Res Bull*, 1999, **34**, 2319–2325.
- 130 K. Ushizawa, K. Watanabe, T. Ando, I. Sakaguchi, M. Nishitani-Gamo, Y. Sato and H. Kanda, *Diam Relat Mater*, 1998, **7**, 1719–1722.
- 131 F. Cerdeira, T. A. Fjeldly and M. Cardona, *Phys Rev B*, 1973, **8**, 4734–4745.
- 132 L. Bergman and R. J. Nemanich, *J Appl Phys*, 1995, **78**, 6709–6719.
- 133 I. Duo, C. Levy-Clement, A. Fujishima and C. Comninellis, *J Appl Electrochem*, 2004, **34**, 935–943.
- 134 D. Liu, L. Gou, J. Xu, K. Gao and X. Kang, *Vacuum*, 2016, **128**, 80–84.
- 135 W. Zhang, Z.-H. Huang, G. Cao, F. Kang and Y. Yang, *J Power Sources*, 2012, **204**, 230–235.
- 136 S. Suman, D. K. Sharma, O. Szabo, B. Rakesh, M. Marton, M. Vojs, A. Vincze, S. P. Dutta, U. Balaji, D. Debasish, R. Sakthivel, K. J. Sankaran and A. Kromka, *J. Mater. Chem. A*, 2024, **12**, 21134–21147.
- 137 P. Knittel, F. Buchner, E. Hadzifejzovic, C. Giese, P. Quellmalz, R. Seidel, T. Petit, B. Iliev, T. J. S. Schubert, C. E. Nebel and J. S. Foord, *ChemCatChem*, 2020, **12**, 5548–5557.
- 138 S. Baluchová, A. Taylor, V. Mortet, S. Sedláková, L. Klimša, J. Kopeček, O. Hák and K. Schwarzová-Pecková, *Electrochim Acta*, 2019, **327**, 135025.
- 139 K. Xia, Q. Gao, J. Jiang and J. Hu, *Carbon N Y*, 2008, **46**, 1718–1726.
- 140 T. Kondo, Y. Kodama, S. Ikezoe, K. Yajima, T. Aikawa and M. Yuasa, *Carbon N Y*, 2014, **77**, 783–789.

- 141 C. H. Lee, E. S. Lee, Y. K. Lim, K. H. Park, H. D. Park and D. S. Lim, *RSC Adv*, 2017, **7**, 6229–6235.
- 142 J. Iniesta, P. A. Michaud, M. Panizza, G. Cerisola, A. Aldaz and Ch. Comninellis, *Electrochim Acta*, 2001, **46**, 3573–3578.
- 143 A. M. Román, J. C. Hasse, J. W. Medlin and A. Holewinski, *ACS Catal*, 2019, **9**, 10305–10316.
- 144 A. M. Román, N. Agrawal, J. C. Hasse, M. J. Janik, J. W. Medlin and A. Holewinski, *J Catal*, 2020, **391**, 327–335.
- 145 Z. Liu, S. Baluchová, A. F. Sartori, Z. Li, Y. Gonzalez-Garcia, M. Schreck and J. G. Buijnsters, *Carbon N Y*, 2023, **201**, 1229–1240.
- 146 Z. Szklarz, K. Kołczyk-Siedlecka, E. Vereshchagina, A. Herbjørnrød, P. Wittendorp, S. Jain and P. J. Wójcik, *Materials*, 2024, **17**, 1352
- 147 M. Panizza and G. Cerisola, *Electrochim Acta*, 2003, **48**, 3491–3497.
- 148 Z. Gong, N. Hu, W. Ye, K. Zheng, C. Li, L. Ma, Q. Wei, Z. Yu, K. Zhou, N. Huang, C.-T. Lin and J. Luo, *Journal of Electroanalytical Chemistry*, 2019, **841**, 135–141.